Eur. Phys. J. B **47**, 3–27 (2005)
DOI: 10.1140/epjb/e2005-00303-4

THE EUROPEAN PHYSICAL JOURNAL B

Resonant inelastic X-ray scattering in d and f electron systems

A. Kotani[a]

RIKEN Harima Institute, 1-1-1 Kouto, Mikazuki-cho, Sayo-gun, Hyogo, 679-5148, Japan
and
Photon Factory, Institute of Materials Structure Science, 1-1 Oho, Tsukuba, Ibaraki 305-0801, Japan

Received 10 February 2005
Published online 21 September 2005 –

Abstract. Recent progress in the study of resonant inelastic X-ray scattering (RIXS) spectroscopy in d and f electron systems is described. The main space is devoted to the theoretical investigations, some typical experimental data and the comparison of calculated and experimental results, putting emphasis on the underlying physical mechanisms. We confine ourselves mainly to the studies performed since 2000, and discuss the following topics: (1) RIXS in high T_c cuprates, (2) f^0 and d^0 systems, (3) other transition metal compounds, (4) RIXS by electric quadrupole excitation, and (5) magnetic circular dichroism in RIXS of ferromagnetic systems. Some brief description is also given on the future prospect of the RIXS study.

PACS. 78.70.Ck X-ray scattering – 78.70.Dm X-ray absorption spectra – 78.70.En X-ray emission spectra and fluorescence – 71.27.+a Strongly correlated electron systems; heavy fermions

1 Introduction

Resonant inelastic X-ray scattering (RIXS) is a powerful probe of electronic excitations in condensed matter systems. In RIXS, a core electron is excited, by the incident X-ray, near to the absorption threshold, and then the excited state decays by emitting an X-ray photon. Therefore, RIXS is a second order optical process in contrast to that X-ray photoemission spectroscopy (XPS) and X-ray absorption spectroscopy (XAS) are first order optical processes. The intensity of the signal in RIXS is much weaker than XPS and XAS, because the efficiency of the X-ray emission is quite low, so that high-brilliance X-ray sources are required to obtain precise RIXS experimental data. The recent development in the RIXS study owes to the utilization of the third generation synchrotron radiation as an extremely high-brilliance X-ray source [1–3].

Since RIXS includes the information of both X-ray excitation and X-ray emission inherent in the second order optical process, the information obtained from RIXS is greater than that obtained from the first order optical processes XPS and XAS. Furthermore, RIXS provides us with bulk-sensitive and site-selective information, and the technique of RIXS can be applied equally to metals and insulators. RIXS can be performed in applied electric or magnetic fields, as well as under high pressure, since it is a photon-in and photon-out process [1–3].

Let us consider the RIXS process where an X-ray photon with energy Ω (wave vector $\mathbf{k}_1$) and polarization λ_1 (polarization vector $\mathbf{e}_{\mathbf{k}_1\lambda_1}$) is incident on a material and an X-ray photon with energy ω (wave vector $\mathbf{k}_2$) and polarization λ_2 (polarization vector $\mathbf{e}_{\mathbf{k}_2\lambda_2}$) is emitted due to the electron-photon interaction in the material. The RIXS spectrum is represented by the coherent second order optical formula in the following form [4]:

$$F(\Omega,\omega)=\sum_j\left|\sum_i\frac{\langle j|T_2^{\lambda_2}|i\rangle\langle i|T_1^{\lambda_1}|g\rangle}{E_g+\Omega-E_i+i\Gamma_i}\right|^2 \times\frac{\Gamma_j/\pi}{(E_j+\omega-E_g-\Omega)^2+\Gamma_j^2}\,, \quad (1)$$

where $|g\rangle$, $|i\rangle$, and $|j\rangle$ are initial, intermediate, and final states of the material system, E_g, E_i, and E_j are their energies, Γ_i and Γ_j are the core hole lifetime broadenings in the intermediate and final states, respectively, and $T_1^{\lambda_1}$ and $T_2^{\lambda_2}$ represent optical transition operators. In the soft X-ray region, $T_i^{\lambda_i}(i=1,2)$ is given by the electric dipole (ED) transition

$$T_i^{\lambda_i}\propto\mathbf{e}_{\mathbf{k}_i\lambda_i}\cdot\mathbf{r}, \quad (2)$$

but in the hard X-ray region, the electric quadrupole (EQ) transition

$$T_i^{\lambda_i}\propto i(\mathbf{e}_{\mathbf{k}_i\lambda_i}\cdot\mathbf{r})(\mathbf{k}_i\cdot\mathbf{r}) \quad (3)$$

plays sometimes an important role, in addition to the ED transition.

RIXS is divided into two categories depending on the electronic levels participating the transition of X-ray emission. In the first category, the transition occurs from the valence state to the core state, and we have no core hole left in the final state of RIXS. Typical examples are the $3d$

[a] e-mail: kotani@spring8.or.jp

to $2p$ radiative decay of transition metal elements following the $2p$ to $3d$ excitation by the incident X-ray (denoted as $2p \rightarrow 3d \rightarrow 2p$ RIXS) and the $3d \rightarrow 4f \rightarrow 3d$ RIXS in rare earth elements. In this case, the difference of the incident and emitted X-ray energies (denoted as "Raman shift" or sometimes as "energy loss") corresponds to the energy of electronic elementary excitations, such as the crystal field level excitation, charge transfer excitation, correlation gap excitation and so on[1]. Therefore, RIXS is a powerful probe of measuring the elementary excitations. Compared with the conventional (nonresonant) inelastic X-ray scattering, RIXS has larger intensity and depends on each intermediate state, which is convenient to identify the character of electronic excitations. Furthermore, compared with the optical absorption spectroscopy, the selection rule of detecting electronic excitations in RIXS is different, so that RIXS and optical absorption give complementary information on elementary excitations. For example, the crystal field level excitation is forbidden in optical absorption but allowed in RIXS. If the experimental resolution of RIXS is improved, electronic excitations across the Kondo gap, superconducting gap and so on will also be observed. In the hard X-ray region, the wavelength of X-ray is comparable with the lattice spacing, so that the momentum transfer in RIXS corresponds to the wave number of the excitation mode, so that RIXS provides us with important information on the spatial dispersion of elemental excitations.

The second category of RIXS is the case where the radiative decay occurs from a core state to another core state, so that a core hole is left in the final state of RIXS. Typical examples are the $3p$ to $1s$ radiative decay following the $1s$ to $4p$ excitation in transition metal elements and the $3d$ to $2p$ radiative decay following the $2p$ to $5d$ excitation in rare earth elements. In general, the lifetime of a shallow core hole is longer than that of a deeper one. Further, the lifetime broadening of RIXS is determined by the core hole in the final state, instead of the intermediate state (see Eq. (1)). Taking advantage of these facts, we can detect by RIXS measurements a small signal of core electron excitations which cannot be detected by the conventional XAS measurements because of the large lifetime broadening of a deep core level. We can also obtain by the RIXS measurements the information on the spin-dependence of core electron excitation, which cannot be obtained by the conventional XAS measurements.

The polarization-dependence in RIXS gives important information on the symmetry of electronic states. For linearly polarized incident X-rays, two different polarization geometries, polarized geometry and depolarized geometry, are often used. In both geometries, as shown in Figure 1, the angle of the incident and emitted X-ray directions is fixed at 90°, and the polarization of the emitted X-ray is not detected (because the detection of the emitted X-ray polarization is very difficult in the X-ray region). In the

[1] If the initial and final electronic states are the same in the resonant X-ray scattering process, the incident and emitted X-ray energies are the same and this X-ray scattering process is no more RIXS but resonant "elastic" X-ray scattering.

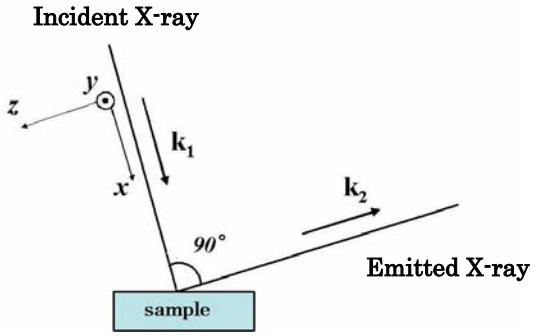

Fig. 1. Polarized and depolarized geometries in RIXS.

polarized geometry, the incident X-ray polarization is perpendicular (y direction) to the scattering plane, while in the depolarized geometry it is parallel (z direction) to the scattering plane. Since the incident X-ray polarization is parallel to the X-ray emission direction in the depolarized geometry, the polarization of X-ray should necessarily be different before and after the scattering. In the polarized geometry, on the other hand, the polarization of the incident X-ray can be the same as that of the emitted X-ray. Another important polarization-dependence in RIXS is the magnetic circular dichroism in ferromagnetic samples. The difference in RIXS for circular polarized incident X-rays with plus and minus helicities gives important information on the magnetic polarization of electronic states in ferromagnetic materials.

Here we would like to mention a few words about terminology. The term of resonant X-ray emission spectroscopy (RXES) or resonant soft X-ray emission spectroscopy (RSXES) is widely used in describing the resonant photon-in and photon-out processes. Strictly speaking, RXES includes more processes than RIXS; the RIXS spectroscopy is a part of RXES which disperses linearly with the incident photon energy, i.e. the part with a constant Raman shift. The term of RXES also includes the resonant elastic X-ray scattering with zero energy loss and "fluorescence" spectroscopy with a constant (or almost constant) X-ray emission energy. If the incident X-ray energy is increased far above the excitation threshold of a core electron, "fluorescence" spectrum is changed into "ordinary fluorescence" spectrum with a strictly constant X-ray emission energy. The spectral shape of the ordinary fluorescence is quite independent of the incident photon energy. In this paper, we confine ourselves mainly to the RIXS spectra of RXES. It is to be mentioned that the RIXS spectroscopy is also called "resonant X-ray Raman spectroscopy" and the ordinary fluorescence spectroscopy is often called "normal X-ray emission spectroscopy (NXES)". The "fluorescence" spectra near the threshold excitation is sometimes called "normal X-ray emission-like (NXES-like) spectra".

In the present paper, we report recent developments in RIXS for d and f electron systems such as transition metal compounds and rare earth compounds. More weight is placed on the theoretical aspects of RIXS than the experimental ones, but lot of space is devoted to the comparison of the theoretical and experimental results of RIXS

spectra in various systems. We confine ourselves mainly to the topics in RIXS performed since 2000, and describe partly some studies before 2000 in subsections of "Background". For more details on the developments in RIXS before 2000, see the review article by Kotani and Shin [2]. For some aspects of recent RIXS studies, one can also refer to short review articles by the present author [5–9].

The organization of the present paper is as follows: in Section 2 we describe some models of electronic states in RIXS calculations for d and f electron systems. Some discussions on RIXS in high T_c cuprates and related materials are given in Section 3, those in f^0 and d^0 systems in Section 4, those in some transition metal compounds in Section 5, and effects of electric quadrupole excitation are discussed in Section 6. In Section 7 we treat magnetic circular dichroism (MCD) in RIXS for ferromagnetic systems. Section 8 is devoted to concluding remarks.

2 Models of electronic states in RIXS calculations

In the RIXS calculations of d and f electron systems, the single impurity Anderson model (SIAM) has been widely used. Since $3d$ or $4f$ electrons in solids are considerably localized spatially with strong correlation, we take into account $3d$ (or $4f$) electron states on a single transition metal ion (or rare earth ion), which hybridize with conduction electron states (in the case of metallic systems) or valence electron states (insulating systems) extended spatially.

For instance, we consider SIAM describing a transition metal oxide. We take into account a single transition metal ion, whose core electron is excited in the RIXS process, and all of the oxygen ions, whose $2p$ states construct the valence band. The Hamiltonian is given by

$$\begin{aligned} H = & \sum_{\Gamma,\sigma} \varepsilon_{d\Gamma}\, a^\dagger_{d\Gamma\sigma}\, a_{d\Gamma\sigma} + \sum_{\mu} \varepsilon_p a^\dagger_{p\mu} a_{p\mu} \\ & + \sum_{\Gamma,k,\sigma} \varepsilon_{\Gamma k} a^\dagger_{\Gamma k\sigma} a_{\Gamma k\sigma} \\ & + \sum_{\Gamma,k,\sigma} V(\Gamma k)(a^\dagger_{d\Gamma\sigma}\, a_{\Gamma k\sigma} + a^\dagger_{\Gamma k\sigma}\, a_{d\Gamma\sigma}) \\ & + U_{dd} \sum_{(\Gamma,\sigma)\neq(\Gamma',\sigma')} a^\dagger_{d\Gamma\sigma}\, a_{d\Gamma\sigma}\, a^\dagger_{d\Gamma'\sigma'}\, a_{d\Gamma'\sigma'} \\ & - U_{dc} \sum_{\Gamma,\sigma,\mu} a^\dagger_{d\Gamma\sigma} a_{d\Gamma\sigma}(1 - a^\dagger_{p\mu}\, a_{p\mu}) \\ & + \frac{1}{2} \sum_{\nu_1,\nu_2,\nu_3,\nu_4} g_{dd}(\nu_1,\nu_2,\nu_3,\nu_4) a^\dagger_{d\nu_1} a_{d\nu_2} a^\dagger_{d\nu_3} a_{d\nu_4} \\ & + \sum_{\nu_1,\nu_2,\mu_1,\mu_2} g_{pd}(\nu_1,\nu_2,\mu_1,\mu_2) a^\dagger_{d\nu_1} a_{d\nu_2} a^\dagger_{p\mu_1} a_{p\mu_2} \\ & + \zeta_d \sum_{\nu_1,\nu_2} (\mathbf{l}\cdot\mathbf{s})_{\nu_1\nu_2} a^\dagger_{d\nu_1} a_{d\nu_2} \\ & + \zeta_p \sum_{\mu_1,\mu_2} (\mathbf{l}\cdot\mathbf{s})_{\mu_1\mu_2} a^\dagger_{p\mu_1} a_{p\mu_2}. \end{aligned} \tag{4}$$

Here the first and second terms on the right hand side represent the $3d$ states (with energy $\varepsilon_{d\Gamma}$) and core states (with p symmetry and with energy ε_p) of transition metal ion, respectively, the third term is the oxygen $2p$ valence band state with energy $\varepsilon_{\Gamma k}$, and the fourth term stands for the hybridization between $3d$ and valence band states, where the index Γ represents the irreducible representation of the local point group symmetry around the transition metal ion, σ is the spin, and μ denotes the combined indices of spin and orbital states. The energy $\varepsilon_{d\Gamma}$ includes the crystal field energy depending on Γ. It is to be noted that the basis state of the oxygen $2p$ valence band is approximately taken to be (Γk) by an appropriate linear combination of Bloch states [10], where $k(=1\sim N)$ is an index representing the energy spread of the valence band instead of the wave vector. The fifth and sixth terms are the spherically averaged Coulomb interaction between $3d$ electrons (U_{dd}) and that between the $3d$ electron and a core hole ($-U_{dc}$), respectively, and the seventh and eighth terms are multi-pole components of these Coulomb interactions. The ninth and tenth terms are the spin-orbit interactions of the $3d$ and core states, respectively.

The Hamiltonian is diagonalized, to obtain the eigenstates $|g\rangle$, $|i\rangle$ and $|j\rangle$ and their energies E_g, E_i and E_j, taking into account the interatomic configuration interaction with a sufficient number of configurations, $3d^n$, $3d^{n+1}\underline{L}$, $3d^{n+2}\underline{L}^2$ ..., where $\underline{L}$ represents a hole in the oxygen $2p$ valence band. The main parameters in this model are the hybridization strength $V(\Gamma)$ (averaged over k), the Coulomb interaction strengths U_{dd} and U_{dc}, and the charge transfer energy defined by

$$\Delta = E(3d^{n+1}\underline{L}) - E(3d^n), \tag{5}$$

where $E(3d^n)$ is the energy averaged over the multiplet terms of the $3d^n$ configuration.

In SIAM, we take into account the contribution of the $2p$ states on all oxygen ions. If we confine ourselves to the contribution of the $2p$ states on those oxygen ions which are located at the neighboring sites of the transition metal ion, SIAM reduces to the "cluster model". The cluster model is also used widely in the analysis of RIXS in transition metal compounds. The Hamiltonean of the cluster model is the same as equation (4), but the oxygen $2p$ valence band states (Γ,k,σ) reduce to the oxygen $2p$ ligand states (Γ,σ), which are the localized molecular orbital states specified by the irreducible representation Γ. Therefore, the cluster model corresponds to SIAM in the limit of vanishing energy width of the oxygen $2p$ valence band.

In the SIAM and the above-mentioned cluster model, we take into account only one transition metal ion, but in some analysis of RIXS, it is necessary to take into account more transition metal sites. In such cases, the cluster model is extended to "multi-site cluster model" which includes multiple transition metal sites. If SIAM is extended to include all the transition metal sites, the resulting model is the so-called periodic Anderson model (or p-d model), but it cannot be solved exactly. The multi-site cluster model corresponds to a finite size version of

the periodic Anderson model so that the exact diagonalization can be made numerically. In most of multi-site cluster models, the multipole components of the Coulomb interaction are disregarded for simplicity.

In the case of rare earth compounds, for instance in rare earth oxides, the SIAM and the cluster model mentioned above can be used simply by replacing the transition metal $3d$ states with the rare earth $4f$ states. In most of rare earth systems, however, the crystal field splitting is too small to play an important role in RIXS structure. Furthermore, the anisotropy in hybridization between the $4f$ and valence band states can also be disregarded, so that the point group around the rare earth ion reduces to SO_3. If the hybridization itself can be disregarded, as actually the case except for some mixed valence materials, the model reduces to "atomic model".

3 RIXS in high T_c cuprates and related materials

3.1 Background

We first describe briefly the study of RIXS in high T_c cuprates before 2000 as a background of recent study. The first theoretical calculation of RIXS for high T_c related cuprates was made by Tanaka and Kotani [11] for Cu $2p \rightarrow 3d \rightarrow 2p$ RXES of La_2CuO_4 with SIAM. The Cu ion in cuprates is nominally in the Cu^{2+} state, but actually the Cu $3d^9$ configuration is strongly mixed with the $3d^{10}\underline{L}$ configuration, where an electron is transferred from oxygen $2p$ valence band to the Cu $3d$ state through the p-d hybridization. As a result, we have the bonding, nonbonding and antibonding states, which are depicted in Figure 2. Furthermore, the bonding state splits into the crystal field levels specified by the irreducible representations of the D_{4h} point group, $\Gamma = b_{1g}, a_{1g}, b_{2g}$ and e_g. The ground state of SIAM is the lowest crystal field state with b_{1g} symmetry (namely, $3d_{x^2-y^2}$ symmetry by taking the two orthogonal Cu-O bond directions as x and y axes). The electronic transition scheme in RIXS is shown in Figure 2; by the incident X-ray the system is excited to the intermediate state with $2p^5 3d^{10}$ configuration, and by emitting X-ray it is de-excited to the final states. If the final state is the same as the ground state, we have the resonant elastic X-ray scattering, while if the final state is the excited states above the ground state, we have the RIXS. Therefore, the RIXS spectrum reflects the crystal field level excitation (denoted by d-d excitation) and the excitations to the nonbonding and antibonding states (denoted by charge transfer (CT) excitation). An example of the RIXS spectrum calculation by Tanaka and Kotani is shown on the right hand side of Figure 2. Here, the RIXS intensity is plotted as a function of the Raman shift (which is defined by the difference of the incident and emitted X-ray energies), where the polarizations of incident and emitted X-rays are both taken in the x direction in the CuO_2 plane. It is to be noted that the Raman shift corresponds to the energy of the elementary excitations. The

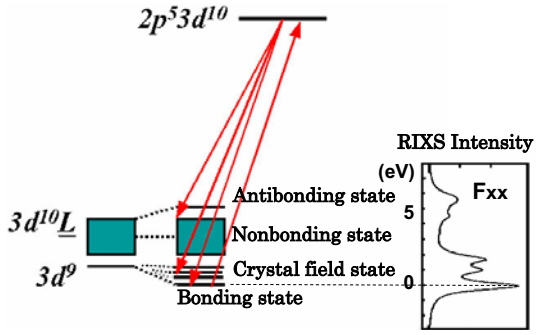

Fig. 2. Schematic transition diagram of the Cu $2p \rightarrow 3d \rightarrow 2p$ RIXS in cuprates and an example of the calculated RIXS spectrum.

peak at the zero Raman shift is the elastic scattering peak, the RIXS features below 2 eV are the d-d excitations, and those around 6 eV are the CT excitations. Tanaka and Kotani also showed that the RIXS spectra depend on the polarization geometry of the incident and emitted X-rays, which reflects the symmetry of the electronic states participating the RIXS process.

A few years after this calculation, Duda [12] succeeded in measuring these RIXS spectra for La_2CuO_4. Although the experimental resolution is not good, the experimental results were in agreement with the calculated ones within the resolution [12,13,60]. These theoretical and experimental studies demonstrated that RIXS is an important tool to detect the d-d and CT excitations in transition metal compounds, and that the polarization dependence in RIXS can provide us with important information on the symmetry of electronic states and electronic excitations.

After Duda's experiments, the RIXS measurements with higher resolution were made by Kuiper et al. [15] for $Sr_2CuO_2Cl_2$ in the d-d excitation range of the Cu $3p \rightarrow 3d \rightarrow 3p$ RIXS, instead of the Cu $2p \rightarrow 3d \rightarrow 2p$ RIXS. Kuiper et al. analyzed the polarization dependence of the observed RIXS spectra and discussed the d-d excitation energies for four different irreducible representations.

Hill et al. [16] measured the Cu $1s \rightarrow 4p \rightarrow 1s$ RIXS for Nd_2CuO_4. An example of the observed RIXS spectra are shown in Figure 3, where the incident X-ray is π polarized (perpendicular to the CuO_2 plane) and its energy is changed in the region of two features of the Cu $1s$ XAS (denoted by features A and B whose energies are around 8990 eV and 8983 eV, respectively). As seen from Figure 3, Hill et al. observed a 6 eV RIXS peak which is resonantly enhanced at the XAS feature A, but almost no resonant enhancement at the feature B (as in the case of the 8980 eV excitation). Theoretical analysis of this RIXS was first made with SIAM [16]. It is shown that the features A and B correspond to the antibonding and bonding states between $\underline{1s}4p3d^9$ and $\underline{1s}4p3d^{10}\underline{L}$ configurations in the intermediate state of RIXS (final state of XAS) and the 6 eV peak corresponds to an antibonding state between $3d^9$ and $3d^{10}\underline{L}$ configurations in the RIXS final state. The calculated result of RIXS can well reproduce the experimental one for the incident X-ray energy

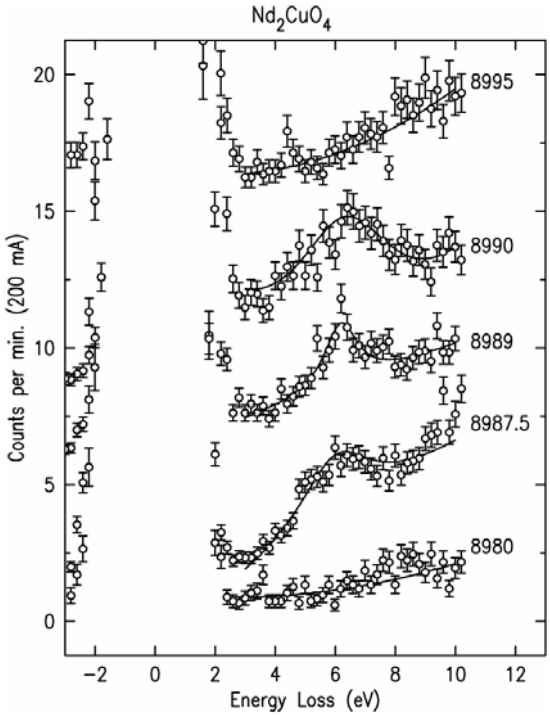

Fig. 3. Experimental data of the Cu $1s \rightarrow 4p \rightarrow 1s$ RIXS of Nd_2CuO_4 shown as a function of energy loss. Data are offset vertically for clarity and the solid curves are guides to the eye. From Hill et al. [16].

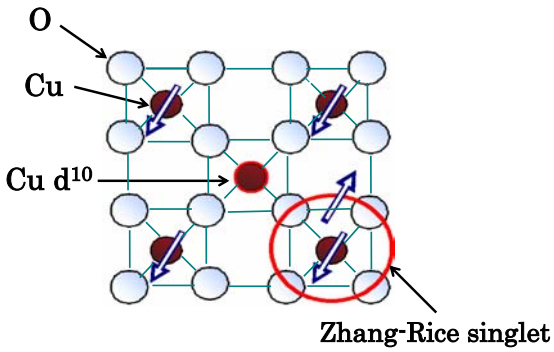

Fig. 4. Schematic illustration of intermediate and final states of the Cu $1s \rightarrow 4p \rightarrow 1s$ RIXS of cuplates with the Cu_5O_{16} cluster model.

around the feature A, but for that around B the calculated result also shows a resonant enhancement of the 6 eV intensity in disagreement with the experimental one.

In order to remove this disagreement, it is necessary to extend the model from SIAM to a model including multiple Cu sites, such as a multi-Cu-site cluster model. The calculation of RIXS with a Cu_5O_{16} cluster model was done by Idé and Kotani [17]. In Figure 4, we show the Cu_5O_{16} cluster. In the ground state, each CuO_4 plaquette includes one hole, whose spin orders antiferromagnetically with down spin ($\downarrow$) on the central plaquette and up spin ($\uparrow$) on the neighboring plaquettes. In the intermediate state, where a Cu $1s$ electron on the central Cu site is

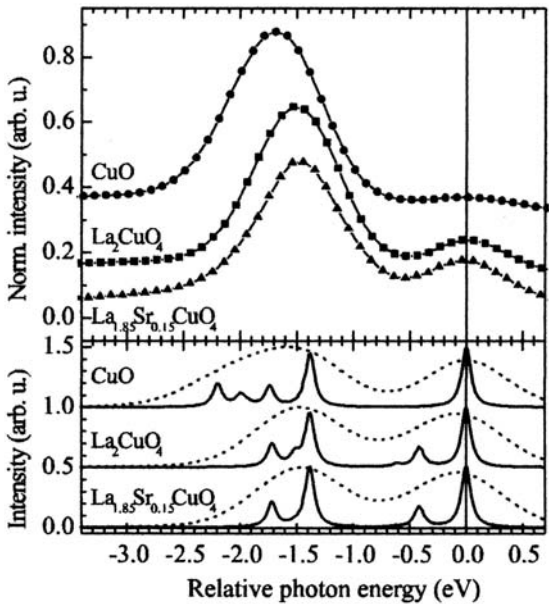

Fig. 5. Experimental RIXS spectra for CuO, La_2CuO_4 and $La_{1.85}Sr_{0.15}CuO_4$ (upper panel) and calculated ones (lower panel) with a 0.05 eV Lorentzian broadening (solid curves) and after a 0.8 eV Gaussian broadening (dashed curves). From Ghiringhelli et al. [19].

excited to the lower energy feature B, an electron is transferred from the neighboring plaquette to the central one to screen the core hole potential. As a result, we have two holes with singlet coupling (denoted by Zhang-Rice singlet state) in the neighboring plaquette, as shown in Figure 4. Then in the final state of RIXS, we also have the state with Cu d^{10} state (with no hole) on the central plaquette and a Zhang-Rice singlet state on the neighboring plaquette. This final state is almost orthogonal with the 6 eV antibonding final state, so that the intensity of the 6 eV peak is strongly suppressed, in agreement with the experiment. The final state in Figure 4 (a pair excitation of Cu d^{10} and Zhang-Rice singlet states) is the low-lying CT excitation state across the correlation gap, and Idé and Kotani [17]. predicted theoretically that this final state would cause a RIXS peak around 2 eV. Unfortunately, in the experiments shown in Figure 3 the 2 eV feature cannot be observed due to the overlap with the high-energy tail of the strong elastic scattering peak. More recent studies on the experimental observation of this type of excitation and its momentum dependence will be discussed in the next subsection.

3.2 More recent study

Very recently Ghiringhelli et al. [19] measured the Cu $2p$-$3d$-$2p$ RIXS for various cuprates: insulating compounds CuO, La_2CuO_4, $Sr_2CuO_2Cl_2$, and optimally doped superconductors $La_{1.85}Sr_{0.15}CuO_4$, $Bi_2Sr_2CaCu_2O_{8+\delta}$, $Nd_{1.85}Ce_{0.15}CuO_4$. The resolution is 0.8 eV. Figure 5 is an example of the results, where the experimental data

for CuO, La_2CuO_4 (polycrystals) and $La_{1.85}Sr_{0.15}CuO_4$ (single crystal) are shown in the upper panel, and the calculated results with a simple crystal field model (point charge model) are shown in the lower panel. The incident X-ray is of 10° grazing incidence with the polarization perpendicular to the scattering plane, while the scattering angle is 70°. Here the *d*-*d* excitation in RIXS is the central issue, and the calculated results after a 0.05 eV Lorentzian broadening are shown with the solid curves and those after a 0.8 eV Gaussian broadening are with the dashed curves. It is seen that the RIXS energy of the *d*-*d* excitation of La_2CuO_4 is, after 0.8 eV broadening, almost unchanged by doping, and somewhat smaller than that of CuO, in agreement with experiments. For instance, the *d*-*d* excitation energies referred to the b_{1g} state for $La_{2-x}Sr_xCuO_4$ are 0.41 eV (for a_{1g}), 1.38 eV (b_{2g}) and 1.51 eV (e_g), and the solid curve in Figure 5 represents these states and their spin flip sates with the flipping energy 0.2 eV. They also measured the polarization dependence (incident polarizations perpendicular and parallel to the scattering plane for both grazing and normal incidence) of the RIXS spectra due to the *d*-*d* excitation and showed that the polarization dependence is well reproduced by their crystal field model. Here it is to be remarked that there are two origins which determine the *d*-*d* excitation energy: the static crystal field effect and the anisotropic hybridization between Cu 3*d* and O 2*p* states. For most of transition metal compounds including cuprates, the effect of the anisotropic hybridization is considered to be more important than the static crystal field. Therefore, more careful studies will be necessary to fully understand the *d*-*d* excitation mechanism. In any case, the polarization dependence (selection rule) of the *d*-*d* excitations in RIXS requires only the symmetry argument, which is the same for both crystal field and hybridization mechanisms.

The study of the Cu $1s \rightarrow 4p \rightarrow 1s$ RIXS has made a remarkable development on the spatial dispersion of the CT excitations. As shown in Figure 4, the final state of RIXS (lower energy excitation than the antibonding CT excitation) includes the d^{10} state (on the central core-excited site) and the Zhang-Rice singlet state (in the neighboring CuO_4 plaquette).

In larger clusters or an infinite system, the d^{10} state and the Zhang-Rice singlet state have a spatial dispersion due to the translational motion of these elementary excitations to form the upper Hubbard band (UHB) and the Zhang-Rice singlet band (ZRB), respectively. Therefore, the RIXS measurements can detect the electron-hole pair excitation, i.e., the electronic excitation from the occupied ZRB to the empty UHB across the correlation gap (denoted hereafter by UHB-ZRB pair excitation). Furthermore, by measuring the dependence of RIXS spectra on the momentum transfer **q**, one can obtain the dispersion of this UHB-ZRB pair excitation. In Figure 6, we show a typical example of experimental results for the **q** dependent RIXS spectra in $Ca_2CuO_2Cl_2$ observed by Hasan et al. [20] In this figure, the RIXS peak around 5.8 eV is due to the antibonding state excitation, which is well localized with almost no energy dispersion, and those on

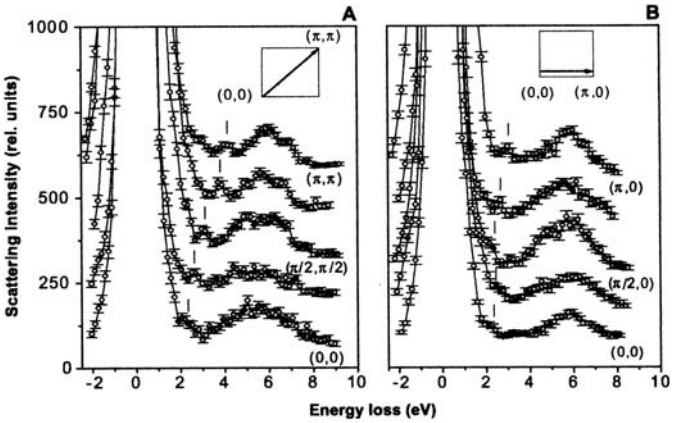

Fig. 6. Experimental results of the **q** dependent Cu $1s \rightarrow 4p \rightarrow 1s$ RIXS spectra for $Ca_2CuO_2Cl_2$, where **q** is in the ⟨110⟩ direction (A) and ⟨100⟩ direction (B). Incident photon energy is 8.996 KeV. From Hasan et al. [20].

the lower energy side (indicated by the vertical bars) are UHB-ZRB pair excitations. The dispersion of the UHB-ZRB pair excitation is anisotropic: in the ⟨110⟩ direction the excitation energy increases from 2.5 eV at $(k_x, k_y) = (0, 0)$ to 3.8 eV at (π, π), while in the ⟨100⟩ direction it changes from 2.5 eV at (0, 0) to 3.0 eV at $(\pi, 0)$.

Theoretical calculations of these energy dispersions were made by exact diagonalization method with a 4 × 4 site cluster model described by a single band Hubbard Hamiltonian (instead of the periodic Anderson Hamiltonian) taking into account the first, second and third nearest neighbor hoppings. The calculated results are in good agreement with the experimental ones. It is to be mentioned that the single band Hubbard model does not include the O 2*p* states, so that the calculated RIXS spectra are due to a pair excitation of an UHB electron and a lower Hubbard band (LHB) hole. We should regard that the calculated LHB states represent effectively the ZRB states in the case of the periodic Anderson model. It is also to be mentioned that energy dispersion of ZRB of various cuprates has been measured extensively by angle resolved photoemission (ARPES) experiments and the results have been analyzed theoretically, but what is measured in RIXS is not the single particle (a hole in ZRB) excitation spectrum but the UHB-ZRB pair excitation spectrum. The pair is not necessarily a free pair but in general a coupled pair, which can form an exciton-like bound state [21]. In this point, RIXS provides more information than ARPES, in addition to the advantage that RIXS is a more bulk sensitive probe than ARPES.

Hasan et al. [22] also measured the momentum-resolved Cu $1s \rightarrow 4p \rightarrow 1s$ RIXS spectra in one-dimensional cuprate systems $SrCuO_2$ and Sr_2CuO_3, where the CuO_4 plaquettes are connected as a one-dimensional chain with sharing the corners of plaquettes. The observed momentum dependence of the UHB-ZRB pair was found to be more dispersive than that of the two-dimensional cuprate $Ca_2CuO_2Cl_2$. This result is very interesting because the trend is quite opposite to that in a simple

energy band picture of uncorrelated electron systems; within a one-body energy band model the dispersion of one-dimensional energy band is smaller than that of two-dimension energy band due to the smaller number of neighboring atoms, if the hopping integrals are the same (actually the Cu $3d$-O $2p$ hopping strength should be very similar for $SrCuO_2$, Sr_2CuO_3 and $Ca_2CuO_2Cl_2$). In strongly correlated cuprates, on the other hand, the hopping of charge carriers (an electron in UHB and a hole in ZRB) is more difficult in two-dimensional lattice with antiferromagnetic 1/2 spin arrangement than in one-dimensional one, because the hopping of the charge carrier induces the change of the spin arrangement around the carrier in the two-dimensional lattice, but this is not the case in the one-dimensional lattice due to the separation of spin and charge degrees of freedom. Theoretical calculations of RIXS spectra in one-dimensional and two-dimensional insulating cuprates have been made by Tsutsui et al. [23,24] using the exact diagonalization technique for extended Hubbard model, and the results are consistent with the experimental ones by Hasan et al. It is considered that a photo-created hole in the one-dimensional Zhang-Rice singlet band cannot exist as a quasiparticle but changes into two collective excitations, a spinon and a holon, as discussed by Kim et al. [25] On the other hand, Nomura and Igarashi [26] calculated recently the momentum dependence of RIXS spectra of quasi-one-dimensional cuprates by quite a different approach, where the antiferromagnetic ground state is described weithin the Hartree-Fock theory and the CT excitation is calculated within the random phase approximation.

Further measurements of the momentum-resolved Cu $1s \rightarrow 4p \rightarrow 1s$ RIXS spectra and their interpretations have been made by Kim et al. [27–29] for two-dimensional cuprate La_2CuO_4, one-dimensional corner-sharing cuprate $SrCuO_2$, and one-dimensional edge-sharing cuprate Li_2CuO_2. The result for La_2CuO_4 exhibits some features which have not been observed in $Ca_2CuO_2Cl_2$ by Hasan et al. [20]. Kim et al. [27] observed for La_2CuO_4 two highly dispersive CT excitations, in addition to the antibonding excitation at about 7.3 eV. The low-energy mode has a gap of 2.2 eV and band width of 1.0 eV, and shows a strong $\mathbf{q}$-dependent intensity variation, while the second peak shows a smaller dispersion of about 0.5 eV with a zone-center energy of about 3.9 eV. The former corresponds to the UHB-ZRB pair excitation (forming an exciton-like state), while the latter might be another UHB-ZRB pair with different symmetry or another exciton-like mode. Kim et al. [30] also made similar RIXS measurements for hole-doped $La_{2-x}Sr_xCuO_4$ with $x = 0.05$ and 0.17. The result for $x = 0.05$ sample is similar to the undoped La_2CuO_4 ($x = 0$), but for the sample with $x = 0.17$ they observed the appearance of a continuum of intensity below 2 eV and the spectral weight transfer from the lowest-lying CT excitation of the $x = 0$ sample to the continuum intensity below the gap. The gap-filling continuum excitation is considered to arise from the incoherent particle-hole pairs creation near the Fermi surface. In contrast to this, the second peak and the highest antibonding excitation are not very much affected by doping except for some change of the excitation energy.

In this connection, Kim et al. [31] have made systematic measurements of the antibonding excitation energy for a wide variety of cuprate compounds, including doped and undoped La_2CuO_4. They observed for about 10 different cuprate compounds a systematic trend that the excitation energy increases with the decrease in the Cu-O bond length d. For instance, the excitation energy is about 5.7 eV for Nd_2CuO_4 with $d = 1.97$ Å, about 7.3 eV for La_2CuO_4 with $d = 1.90$ Å, and about 7.7 eV for $La_{1.83}Sr_{0.17}CuO_4$ with $d = 1.88$ Å. This trend is reasonable from a simple picture shown in Figure 2, because the decrease in d causes the increase of the Cu $3d$-O $2p$ hybridization strength, resulting in the increase in the energy separation of the antibonding and bonding states. At the same time, they observed some features showing a deviation from the simple picture; The observed excitation energy is proportional to d^{-8}, while the simple picture and a simple relation [32] between the hybridization strength and d predicts that it is proportional to $d^{-3.5}$. Furthermore, the observed excitation energy shows some momentum dependence, which increases significantly with the decrease of d, indicating that the antibonding-bonding excitation is not necessarily well localized but has some energy dispersion due to the effect of the translational symmetry.

Recently, the study of RIXS for cuprates are extended from that on the Cu site to that on the O site [33–36]. The experimental results of the O site derived RIXS have mainly been interpreted based on the partial O $2p$ density of states obtained by energy band calculations [37]. Duda et al. [33] first pointed out that in their O $1s \rightarrow 2p \rightarrow 1s$ RIXS spectra, which were observed for $CuGeO_3$, the d-d excitation signal was recognized similarly to that in the RIXS at the Cu p edge. Okada and Kotani [34,35] have shown by their theoretical calculations that even in the RIXS by the O site excitation (O $1s \rightarrow 2p \rightarrow 1s$ RIXS) the many body effects, such as the Cu d-d excitation, the CT excitation and the UHB-ZRB pair excitation, should be reflected in RIXS, because of the strong hybridization between Cu $3d$ and O $2p$ states.

In Figure 7 the calculated result for the O $1s \rightarrow 2p \rightarrow 1s$ RIXS with Cu_4O_{13} cluster model (corresponding to an undoped cuprate) is shown, where the incident X-ray energy is tuned at the peak position of XAS [35]. In this calculation two different polarization geometries, polarized and depolarized geometries, with the incident X-ray normal to the CuO_2 plane is taken into account. It is shown that the 6 eV antibonding CT excitation and the UHB-ZRB pair excitation, as well as the d-d excitation (indicated as "$dd(xy)$ and $dd(xz)$") and a spin flip excitation, can be clearly seen, in addition to the most prominent RIXS peak which corresponds to the nonbonding CT excitation. The CT excitation and the UHB-ZRB pair excitation depend on the polarization direction of the incident X-ray because of the symmetry selection rule. Experimental observation corresponding to this calculation has also been made by Harada et al. [35] for $Sr_2CuO_2Cl_2$ with

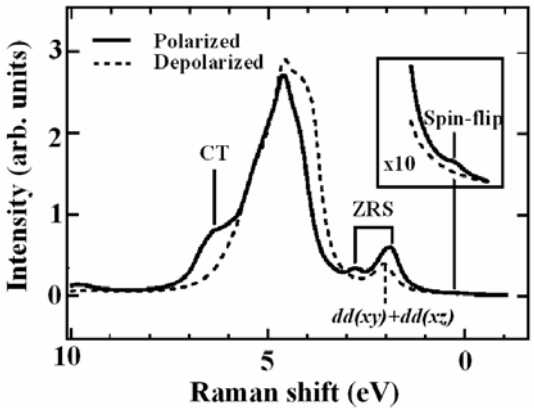

Fig. 7. Calculated results of the O $1s \rightarrow 2p \rightarrow 1s$ RIXS with a Cu_4O_{13} cluster model. In the inset, the intensity is enlarged 10 times. From Harada et al. [35].

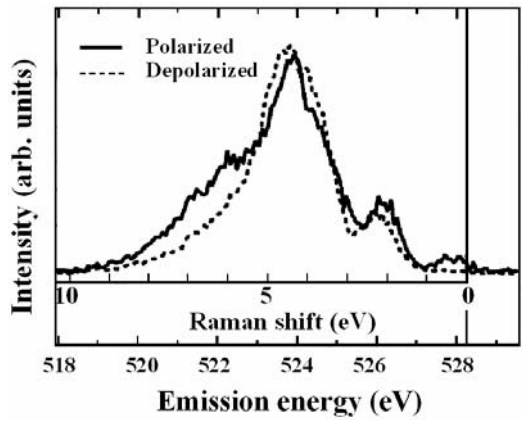

Fig. 8. Experimental results of the O $1s \rightarrow 2p \rightarrow 1s$ RIXS for $Sr_2CuO_2Cl_2$. From Harada et al. [35].

almost the same geometry, and the result is shown in Figure 8. The experimental result is in satisfactory agreement with the calculated one.

Here we would like to mention the difference in the UHB-ZRB pair excitation mechanism in RIXS with the Cu site excitation (Cu $1s \rightarrow 4p \rightarrow 1s$ RIXS) and that with the O site excitation (O $1s \rightarrow 2p \rightarrow 1s$ RIXS). In the former RIXS, the UHB-ZRB pair excitation is formed in the intermediate and final states as seen in Figure 4. In the latter RIXS, on the other hand, the UHB-ZRB pair excitation is not formed in the intermediate state and occurs only in the final state of RIXS. In Figure 9, we show schematically the process of the UHB-ZRB pair excitation [34]. In the ground state (top panel), we have a hole (hybridized Cu $3d$ and O $2p$ hole with b_{1g} symmetry) in each CuO_4 plaquette (this hybridized state is written symbolically as "b_{1g}" state), and their spin is ordered antiferromagnetically ("b_{1g}" $\uparrow$ and "b_{1g}" $\downarrow$ states in the right and left hand plaquettes in Fig. 9). We assume, as shown in the figure, that an O $1s$ electron with $\uparrow$ spin on the central O site is excited to the O $2p_x \uparrow$ state by the x-polarized incident X-ray. Then in the intermediate state (middle panel), we have an O $1s \uparrow$ hole, an O $2p_x \uparrow$ electron and a "b_{1g}" $\downarrow$ hole. In the X-ray emission process, an O $2p_x$ or $2p_y$ or $2p_z$

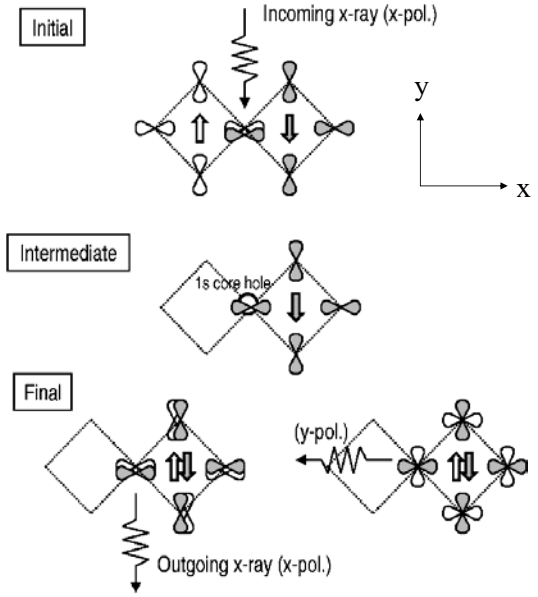

Fig. 9. Illustration of the O $1s \rightarrow 2p \rightarrow 1s$ RIXS process. With x polarized incident and emitted X-rays, the Z-R singlet state is formed in the right hand side CuO_4 plaquette (see the left hand side of the lowest panel.) From Okada and Kotani [34].

electron with $\uparrow$ spin on the central O site can recombine with the O $1s \uparrow$ hole, and we have various final states depending on the emitted X-ray polarization. If the emitted polarization is in the x direction, for example, one of the typical final states is that shown on the left hand side of the bottom panel, where we have two holes with "b_{1g}" $\uparrow$ and "b_{1g}" $\downarrow$ states bound on the right hand plaquette and no hole on the left hand plaquette. This is nothing but the UHB-ZRB pair excitation. If the emitted polarization is in the y direction, however, the UHB-ZRB pair final state is forbidden, but two holes with "b_{2g}" $\uparrow$ and "b_{1g}" $\downarrow$ states bound on the right hand plaquette can be formed. In this way, the final states of RIXS strongly depend on incident and emitted X-ray polarizations. It can also be seen, as another example of the selection rule, that the elastic scattering where the final state is the same as the ground state is allowed for x polarized incident and x polarized emitted X-rays, but is forbidden for the x polarized incident and y polarized emitted X-rays.

4 f^0 and d^0 systems

In La compounds, the $4f$ level is unoccupied because it is located well above the Fermi level, so that they are called the $4f^0$ system. On the other hand, the mixed valence Ce compounds such as CeO_2 are called "nominally $4f^0$ system", but actually the $4f^0$ and $4f^1\underline{L}$ configurations are strongly mixed in the ground state, forming the bonding, nonbonding and antibonding states. The situation is similar to that in Figure 2, if we replace the Cu $3d^9$ and $3d^{10}\underline{L}$ configurations by the Ce $4f^0$ and $4f^1\underline{L}$ configurations, respectively, although the crystal level splitting is too small to be observed by RIXS experiments. The

intermediate states of the Ce $3d \rightarrow 4f \rightarrow 3d$ RIXS of CeO_2 are also the mixed states (bonding and antibonding states) of the $3d^9 4f^1$ and $3d^9 4f^2 \underline{L}$ configurations with the energy separation of about 6 eV.

Transition metal compounds, such as ScF_3, TiO_2, V_2O_5, are the nominally $3d^0$ systems. For instance for TiO_2, the initial and final states of RIXS are mixed states of the Ti $3d^0$ and $3d^1\underline{L}$ configurations, and the intermediate states are mixed states of Ti $2p^5 3d^1$ and $2p^5 3d^2 \underline{L}$ configurations, so that the situation is similar to that in the Ce $3d \rightarrow 4f \rightarrow 3d$ RIXS of CeO_2 by replacing the Ce $3d$ and $4f$ states with the Ti $2p$ and $3d$ states, respectively. Quantitatively, however, the hybridization strength between Ti $3d$ and O $2p$ states in TiO_2 is much larger than that between Ce $4f$ and O $2p$ states in CeO_2, so that the energy separation of the antibonding and bonding states in both intermediate and final states of RIXS in TiO_2 is about 14 eV, which is much larger than that in CeO_2 (about 6 eV in the intermediate state and about 7 eV in the final state).

4.1 Background

The first experimental measurement of the Ce $3d \rightarrow 4f \rightarrow 3d$ RIXS of CeO_2 was made by Butorin et al. [40], and the results were analysed by SIAM. The measurements were done only in the polarized geometry, and RIXS spectra exhibit double-peak structure: For the incident energy resonating with the lower energy peak of XAS (bonding intermediate state between $3d^9 4f^1$ and $3d^9 4f^2 \underline{L}$ configurations) the RIXS spectrum has two peaks of bonding and nonbonding final states with the energy separation of about 5 eV and for the incident energy at the higher XAS peak (antibonding intermediate state) the RIXS spectrum has two peaks of bonding and antibonding final stats (separated by about 7 eV), where the bonding final state corresponds to the elastic line.

For TiO_2, Jiménez-Mier et al. [41] measured the Ti $2p \rightarrow 3d \rightarrow 2p$ RIXS only in the depolarizred geometry. For details see the original paper and the review article [2]. Before 2000, the drastic polarization dependence in f^0 and d^0 systems was not recognized, so that the RIXS for CeO_2 by Butorin et al. was measured only in the polarized geometry, and that for TiO_2 by Jiménez-Mier et al. was only in the depolarized geometry.

4.2 Drastic polarization dependence in TiO_2

The polarization dependence in the Ti $2p \rightarrow 3d \rightarrow 2p$ RIXS of TiO_2 was calculated by Matsubara et al. [42] and measured by Harada et al. [43]. The calculation of RIXS spectra is made with the TiO_6 cluster model with O_h symmetry [42]. The results are shown in Figure 10, where the Ti $2p \rightarrow 3d$ XAS and $2p \rightarrow 3d \rightarrow 2p$ RIXS are shown in Figures 10a and 10b, respectively. The incident photon energy in RIXS is taken at the positions **a**-**h**, in the XAS spectrum. The spectral structure is divided into three categories: (1) elastic line at 0 eV, (2) inelastic spectra at 7 and 9 eV, and (3) inelastic line at 14 eV. The mechanism of these spectra can be explained by the energy level scheme shown in Figure 11. The ground state of TiO_2 is the bonding state between the $3d^0$ and $3d^1\underline{L}$ configurations, and the antibonding state is located about 14 eV above the ground state. Both bonding and antibonding states are specified by irreducible representation A_{1g} of the O_h symmetry group. In addition to these states, there are nonbonding $3d^1\underline{L}$ states with $T_{1g}, T_{2g}, E_g \cdots$ symmetries about $7 \sim 9$ eV above the ground state. When a Ti $2p$ electron is excited to the $3d$ state by the incident photon, we have $2p^5 3d^1$ and $2p^5 3d^2 \underline{L}$ configurations which are mixed strongly by the covalency hybridization. The main peak of the Ti $2p$ XAS corresponds to the bonding state between the $2p^5 3d^1$ and $2p^5 3d^2 \underline{L}$ configurations, while the satellite corresponds to the antibonding state between them. The intensity of the satellite is very weak

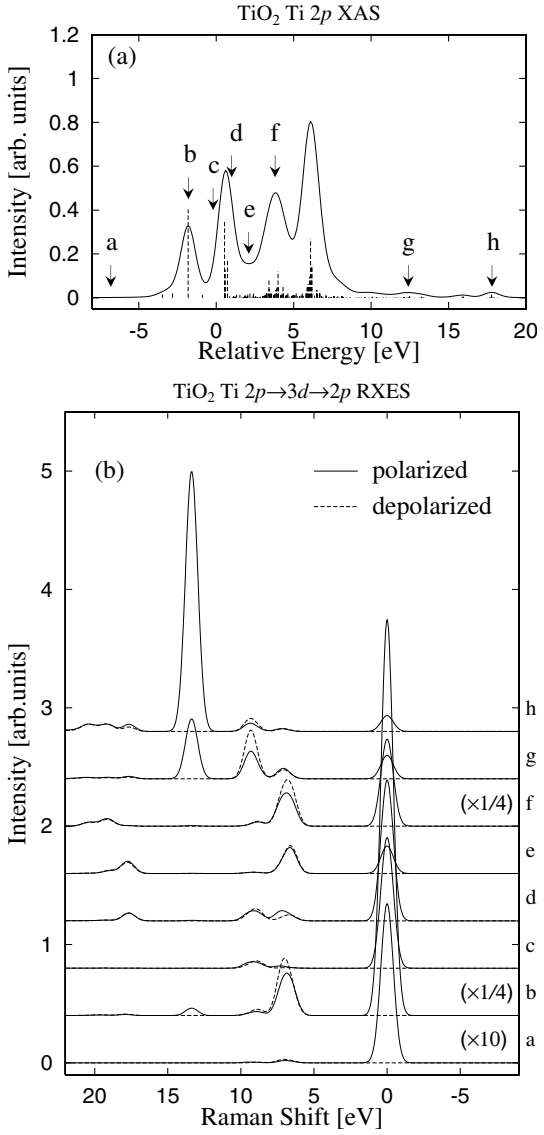

Fig. 10. Calculated results of (a) Ti $2p$ XAS and (b) Ti $2p \rightarrow 3d \rightarrow 2p$ RIXS of TiO_2 with TiO_6 cluster model. From Matsubara et al. [42].

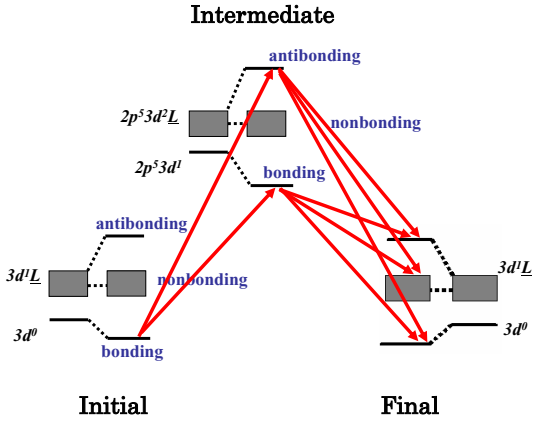

Fig. 11. Schematic representation of the Ti $2p \rightarrow 3d \rightarrow 2p$ RIXS transition of TiO_2.

because of the phase cancellation between the wave functions of the ground and photo-excited states [44]. Also, the X-ray absorption is almost forbidden to the nonbonding $2p^5 3d^2\underline{L}$ states.

In Figure 11, we disregard the effects of the spin-orbit splitting of the $2p$ states and the crystal field splitting of the $3d$ states, for simplicity. If we take into account these effects, the main peak (and also the satellite) splits into four peaks.

The resonantly excited intermediate states, which correspond to the main peak and the satellite of the XAS, decay radiatively to each final state of RIXS, i.e., the bonding, nonbonding, and antibonding states. The categories (1), (2), and (3) of the calculated spectra correspond to the bonding, nonbonding, and antibonding final states, respectively. The spectrum (2) has two peaks, which correspond to the crystal field splitting of the nonbonding $3d^1\underline{L}$ configuration ($3d^1(t_{2g})\underline{L}$ and $3d^1(e_g)\underline{L}$). The spectrum (3) occurs for the incident photon energy tuned to the satellite of the XAS spectrum. This is because the XAS satellite corresponds to the antibonding intermediate state of RIXS, so that the intensity of the antibonding final state is dramatically enhanced. The spectra (1) and (3) are allowed only for the polarized geometry, while the spectrum (2) is allowed for both polarized and depolarized geometries.

The mechanism of the polarization dependence of the RIXS spectra is as follows: Here we neglect spin-orbit interaction for simplicity although it is included in the calculation in Figure 10. Since the ground state symmetry of TiO_2 is A_{1g} and the electric dipole transition operator (both for X-ray absorption and emission processes) is represented by T_{1u}, the irreducible representations in the final state is given by reducing the product representation $A_{1g} \otimes T_{1u} \otimes T_{1u}$. In order to obtain the selection rule for the polarized and depolarized geometries, we take the scattering plane as the zx plane and the component of the dipole excitation operator as $T_{1u}(y)$ for the polarized geometry and as $T_{1u}(z)$ for the depolarized geometry, as shown in Figure 1. Then, the irreducible representations allowed in the final state of RIXS are given by

$$\sum_{\gamma=x,y} A_{1g} \otimes T_{1u}(y) \otimes T_{1u}(\gamma) = A_{1g}, E_g, T_{1g}, T_{2g}, \quad \text{(polarized)} \qquad (6)$$

$$\sum_{\gamma=x,y} A_{1g} \otimes T_{1u}(z) \otimes T_{1u}(\gamma) = T_{1g}, T_{2g} \quad \text{(depolarized)}. \qquad (7)$$

Therefore, the elastic peak (bonding state) and the 14 eV inelastic peak (antibonding state) are allowed for the polarized geometry, but they are forbidden for the depolarized geometry. The nonbonding states are allowed both for the polarized and depolarized geometries.

Experimental results of RIXS for TiO_2 is shown in Figure 12. The three categories of RIXS spectra (1) $\sim$ (3) are clearly seen, in addition to the spectra indicated by vertical bars, which are absent in the calculated results (Fig. 10). The elastic scattering peak at 0 eV (category 1) and the inelastic one at 14 eV (category 3) are allowed only for the polarized geometry, and the intensity of the 14 eV peak is dramatically enhanced when the incident photon energy is tuned to the satellite of the XAS spectrum. Near the middle of the elastic (0 eV) and inelastic (14 eV) scattering peaks, there are inelastic scattering spectra (category 2) which are allowed both for the polarized and depolarized geometries. These results are in good agreement with the calculated ones. The spectral width of (2) is much larger than that of the calculated result, and this broadening comes mainly from the energy band width of the O $2p$ states, which is disregarded in the cluster model.

It is to be mentioned that some difference between the calculated and experimental results is seen for the Ti $2p$ XAS: the second peak of the main structure is split into two in the experiment, but only one peak is seen in the calculation. This discrepancy is due to the approximation that the local symmetry around Ti is treated as O_h, but actually it is D_{2h}. The lower symmetry calculation reproduces this splitting correctly [38]. Now we discuss the origin of the spectra indicated by the vertical bars in Figure 12. The energy position of these bars changes almost proportionally to the change of the incident photon energy, so that the emitted photon energy is almost independent of the incident photon energy, similarly to the so-called normal X-ray emission spectroscopy (NXES) which is usually observed for the incident photon energy well above the XAS threshold. In the experimental result in Figure 12, however, these spectra are observed near the XAS threshold, so that we call them "NXES-like spectra". Idé and Kotani [45,46] calculated RIXS with a one-dimensional d-p model (a simplified version of the nominally $3d^0$ system) with multi-transition-metal sites. They showed that NXES-like spectra are absent in the cluster with a single transition metal site, but for larger clusters NXES-like spectra can occur near the XAS threshold because of the existence of spatially extended XAS final states (RIXS intermediate states) due

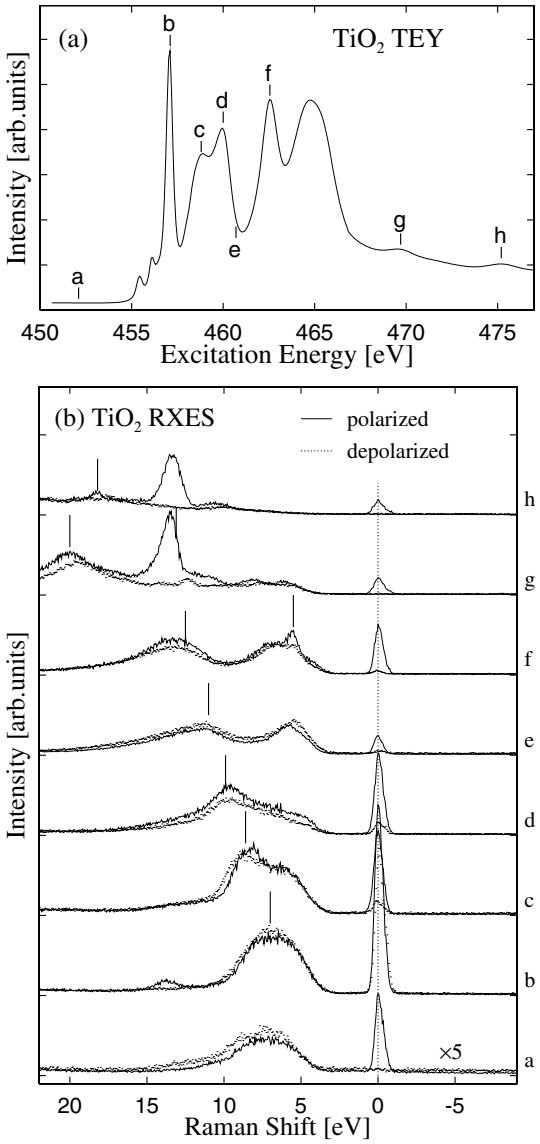

Fig. 12. Experimental results of (a) Ti $2p$ XAS and (b) $2p \rightarrow 3d \rightarrow 2p$ RIXS of TiO_2. From Harada et al. [43].

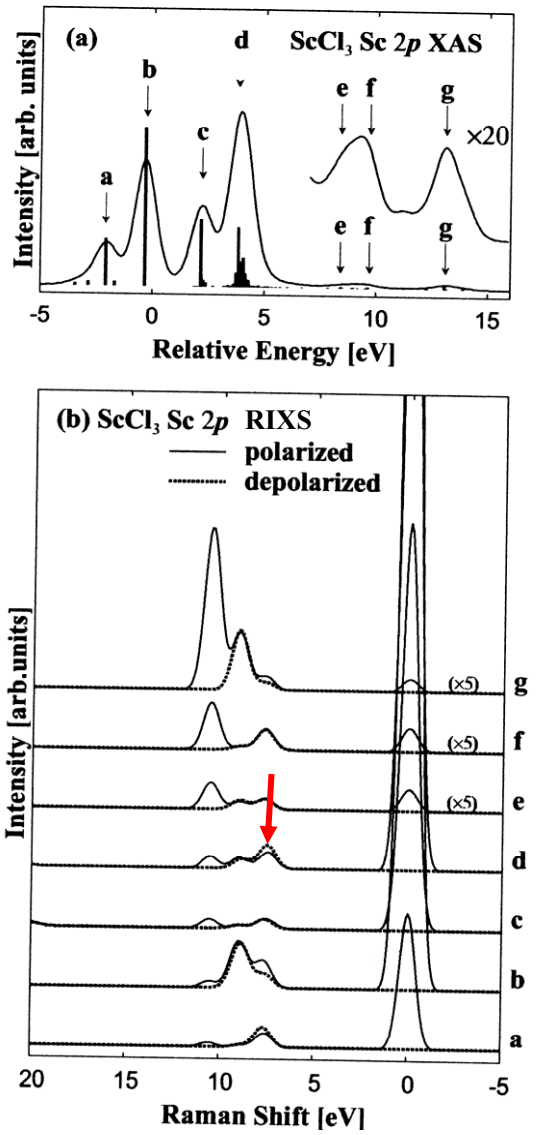

Fig. 13. Calculated results of (a) Sc $2p$ XAS and (b) Sc $2p \rightarrow 3d \rightarrow 2p$ RIXS of $ScCl_3$ with $ScCl_6$ cluster model. From Matsubara et al. [47].

to the effect of of multi-transition-metal sites. Therefore, in order to reproduce the NXES-like spectra of TiO_2, it would be necessary to extend the cluster size to that larger than the TiO_6 cluster.

4.3 Sc compounds and Ce compounds

Sc halides, ScF_3, $ScCl_3$ and $ScBr_3$, are d^0 systems, and the Sc $2p \rightarrow 3d \rightarrow 2p$ RIXS of these compounds were calculated by Matsubara et al. [42,47] with the ScX_6 (X = F, Cl and Br) cluster model, similarly to the calculations for TiO_2. The results for $ScCl_3$ are shown in Figure 13. The main difference in the electronic states of Sc halides and TiO_2 is that the CT energy Δ of Sc halides is much larger than that of TiO_2. As a result, the nonbonding excitation energies in RIXS of Sc halides is very close to the antibonding excitation energy; for instance in $ScCl_3$, as seen from Figure 13, the nonbonding excitation energies are about 7.5 eV and 8.5 eV (for $3d^1\underline{L}$ states with $3d(t_{2g})$ and $3d(e_g)$, respectively) and the antibonding excitation energy is about 10.5 eV. The selection rule for the polarized and depolarized geometries is the same as that in TiO_2, but the experimental measurements of RIXS for Sc halides have so far been made only in the depolarized geometry [47]. An interesting point found from the theoretical calculation is that when the incident X-ray energy is tuned to the $\underline{2p_{1/2}}3d^1(e_g)$ peak (shown by **d** in Fig. 13a) of XAS the nonbonding $3d^1(e_g)\underline{L}$ final state is resonantly enhanced for ScF_3, but for $ScCl_3$ and $ScBr_3$ the nonbonding $3d^1(t_{2g})\underline{L}$ final state (shown with the arrow in Fig. 13b) is resonantly enhanced. This anomaly in the resonant enhancement was also confirmed by experimental observations [47], and explained theoretically by that the

$3d$ state in the $2p_{1/2}3d^1(e_g)$ XAS peak is almost pure e_g state for ScF_3, but it is a strong mixture between e_g and t_{2g} states for $ScCl_3$ and $ScBr_3$ because of the stronger hybridization effect, as well as the multiplet coupling effect. In the experimental data for TiO_2 shown in Figure 12b, the nonbonding final state of RIXS is not split into two peaks (t_{2g} and e_g states), so that it is not clear whether the resonance behavior of the nonbonding final state is similar to ScF_3 or $ScCl_3$.

For f^0 systems, the drastic polarization dependence in CeO_2, where only the nonbonding final state is allowed for the depolarized geometry, whereas the bonding, nonbonding and antibonding final states are allowed for the polarized geometry, was theoretically shown by Nakazawa et al. [48], and confirmed experimentally by Watanabe et al. [49]. Even for metallic mixed valence Ce compounds, the selection rule is considered to be essentially the same. This is because the calculations of X-ray spectroscopy in metallic mixed valence Ce compounds are essentially the same as those in insulating mixed valence Ce compounds like CeO_2 only if we replace the completely filled valence band (O $2p$ band for CeO_2) by the metallic conduction band below the Fermi energy. For details see the paper by Kotani et al. [50]. The effect of electron-hole pair excitations across the Fermi level, which is characteristic of metallic systems, gives only higher order corrections with respective to the $1/N_f$ expansion, where $N_f(=14)$ is the spin and orbital degeneracy of the $4f$ state. Nakazawa et al. [51] discussed the higher order correction in the calculation of RIXS spectra.

Dallera et al. [52] measured the polarization dependence in the Ce $3d \rightarrow 4f \rightarrow 3d$ RIXS of intermetallic Ce compounds, $CeRh_3$, $CePd_3$, Ce_7Rh_3 and $CeAl_2$. They observed large polarization dependence for the incident polarizations parallel and perpendicular to the scattering plane, although the resolution is not very good and the scattering angle is somewhat deviated from 90°. They found that the integrated intensity of the dichroism (difference in the signal for the two polarizations) depends on the degree of hybridization between the $4f$ and conduction electron states, so that it can be a bulk-sensitive probe of the weight of the $4f^0$ and $4f^1$ configurations in the ground state. Dallera et al. [53] also measured the polarization dependence in the Ce $3d \rightarrow 4f \rightarrow 3d$ RIXS in the α (20 K) and γ (300 K) phases of the solid solution of Sc (7 at.%): Ce. Reflecting the change in the hybridization strength in the α and γ phases, the polarization dependence changes as expected. In their experimental results, however, the linear dichroism is essentially zero in the α phase, in disagreement with the theoretical expectation, and this requires more detailed study in future.

The Ce $3d \rightarrow 4f \rightarrow 3d$ RIXS, as well as $4d \rightarrow 4f \rightarrow 4d$ RIXS, of the heavy fermion compound CeB_6 was measured by Magnuson et al. [54] in the depolarized geometry, and analyzed theoretically with SIAM. The observed 4 eV and 6 eV RIXS structures are interpreted as originating from the charge transfer excitation to the $4f^2$ final state. Theoretical calculation predicted an additional 2.5 eV RIXS structure ($4f^0$ final state), which was not observed in their experiments but expected to be observed in the polarized geometry, as an indication of the Kondo singlet ground state.

5 Other transition metal compounds

Extending the study for the d^0 systems, the polarization dependence in $2p \rightarrow 3d \rightarrow 2p$ RIXS of transition metal compounds are studied for d^n systems with $n = 1$, 2 and 3 (TiF_3, VF_3 and Cr_2O_3) both theoretically and experimentally by Matsubara et al. [55] From group theoretical consideration, it is seen that the bonding and antibonding final states are forbidden for Cr_2O_3 (with A_{2g} ground state) in the depolarized geometry (as in the case of d^0 system), but they are allowed for TiF_3 (with T_{2g} ground state) and VF_3 (with T_{1g} ground state) even in the depolarized geometry. Generally, with increasing the $3d$ electron number n, the spectral structure of RIXS becomes more complicated because of the crystal field and multiplet coupling effect. On the other hand, the polarization dependence of RIXS, as well as the strength of the antibonding resonance, is shown to become weaker with increasing n, due to the decreasing hybridization effect and the increasing energy spread of the multiplet structures. As a result, the polarization dependence in d^n ($n = 1, 2, 3$) systems is less drastic than that in d^0 systems, even for Cr_2O_3 with essentially the same selection rule as TiO_2.

The V $2p \rightarrow 3d \rightarrow 2p$ RIXS of V compounds, V_2O_3, VO_2, NaV_2O_6 and V_6O_{13}, were measured by Schmitt et al. [56–58] and some of the results were theoretically analyzed by cluster model calculations and energy band calculations of the density functional theory. For a Mott insulator NaV_2O_6, for instance, a sharp RIXS peak at about 1.7 eV and a broad RIXS peak around 6.5 eV are observed and assigned to the d-d excitation and the CT excitation, respectively [56,57]. In Figure 14 we show the experimental data of the V $2p$ XAS (upper panel) and the V $2p \rightarrow 3d \rightarrow 2p$ RIXS (dots in the lower panel) of NaV_2O_6 measured by Schmitt et al. [57] The theoretical results of RIXS calculated with the cluster model is also shown with the solid curves in the lower panel. More recently, very similar RIXS spectra with a sharp peak at 1.6 eV and a broad one around 7 eV have been observed for mixed valence compound V_6O_{13}, and naturally assigned to the d-d excitation and the CT excitation, respectively, quite consistently with the cluster model calculations [58]. On the other hand, very similar RIXS spectra were measured for NaV_2O_6 by Zhang et al. [59], but the lower energy peak (they denoted it as "–1.56 eV energy loss feature") is interpreted in a different way. Zhang et al. calculated the RIXS spectrum with a ladder model consisting of eight V atoms, where only the V d_{xy} orbital is taken into account with on-site and inter-site correlations. They interpreted, based on their calculation, that the relevant RIXS peak is due to the excitation between the lower and upper Hubbard bands. On the controversy of this issue, see the comment by Duda et al. [60], that by van Veenendaal and Fedro [61], and the reply by Zhang et al. [62].

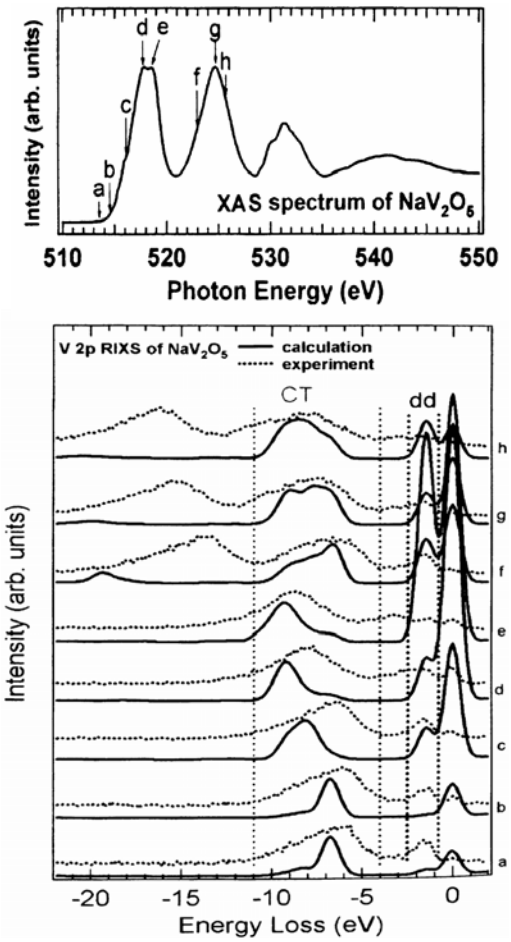

Fig. 14. Experimental data of the V $2p$ XAS (upper panel) and the V $2p \rightarrow 3d \rightarrow 2p$ RIXS (dots in the lower panel) of NaV_2O_6. The incident X-ray energies **a** to **h** are indicated in the upper panel. The RIXS spectra calculated with the cluster model are shown with the solid curves in the lower panel. From Schmitt et al. [57].

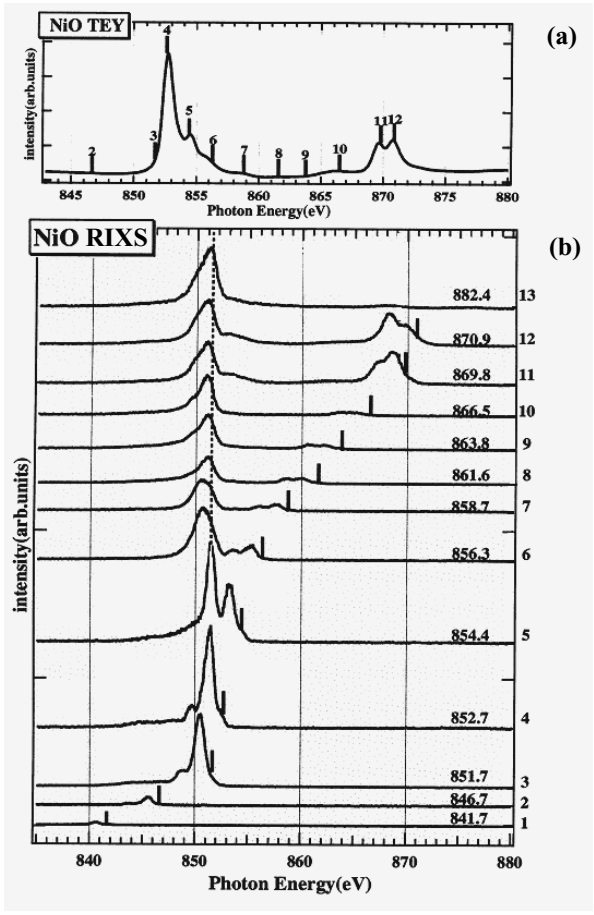

Fig. 15. Experimental results of (a) Ni $2p$ XAS obtained by the total electron yield (TEY) method and (b) Ni $2p \rightarrow 3d \rightarrow 2p$ RIXS for NiO. From Ishii et al. [69].

Spin, charge and orbital orderings in perovskite-type manganites are attracted much attention as effects of strong electron correlation in solids. $LaMnO_3$ is a Mott insulator, where the occupied $3d(e_g)$ states exhibit the orbital ordering below 780 K. Inami et al. [63] measured the Mn $1s \rightarrow 4p \rightarrow 1s$ RIXS of orbitally ordered $LaMnO_3$. They observed three RIXS features at 2.5, 8 and 11 eV. The two higher energy features are interpreted as the CT excitations from O $2p$ bands to the Mn $3d$ and $4s/4p$ bands, while the 2.5 eV peak is ascribed to an orbital excitation across the Mott gap. In the ground state, the occupied e_g states of $3d_{3x^2-r^2}$ and $3d_{3y^2-r^2}$ orbitals are alternatively ordered corresponding to the lower Hubbard band states, so that the relevant orbital excitation occurs from these occupied orbitals to the empty e_g states of $3d_{y^2-z^2}$ and $3d_{z^2-x^2}$ orbitals to form the double occupancy of e_g states (upper Hubbard band) and a hole in the lower Hubbard band. Theoretical calculations were also made for this 2.5 eV peak, and the small momentum dispersion of this peak, as well as the characteristic azimuthal angle dependence, was reproduced considerably well.

For CoO, Magnuson et al. [64] measured the Co $2p \rightarrow 3d \rightarrow 2p$ RIXS spectra and performed the analysis of the spectra with SIAM. They observed both d-d and CT excitations, the latter of which occurs when the incident X-ray energy resonates with the CT satellite of the Co $2p$ XAS in a similar way to that in NiO mentioned in some detail in the next paragraph. Magnuson et al. [65] also measured the temperature dependence of the Co $2p \rightarrow 3d \rightarrow 2p$ RIXS spectra of $LaCoO_3$, which is expected to show a temperature-induced transition of the spin magnetic moment. In this material the NXES-like spectra are mainly observed, probably reflecting delocalized Co $3d$ states. The measured spectra suggest a change in spin state of $LaCoO_3$ as the temperature is raised from 85 to 300 K, while the system remains in the same spin state as the temperature is further increased to 510 K. For CoO, the effect of intra-atomic configuration interaction is investigated both experimentally and theoretically for Co $2p \rightarrow 3d$ excitation and $3s \rightarrow 2p$ radiative transition by Braicovich et al. [66] Similar studies have also been made by Taguchi et al. [67,68] for NiO, $MnFe_2O_4$ and $CoFe_2O_4$.

NiO is a prototype material of the charge-transfer insulator. The Ni $2p \rightarrow 3d \rightarrow 2p$ RIXS was measured by Ishii et al. [69] and Magnuson et al. [70] with almost the

same result. The result by Ishii et al. is shown in Figure 15, where (a) and (b) are the Ni $2p$ XAS and $2p \rightarrow 3d \rightarrow 2p$ RIXS measured in the depolarized geometry, respectively. The RIXS spectra with 1.1, 1.6 and 3.0 eV from the elastic line position (indicated with the vertical bar) are due to the d-d excitations, although not very well resolved, while the peaks with almost constant emission energy (shown with the dotted line) looks like NXES. Magnuson et al. [70,71] made the calculations of these RIXS spectra with SIAM, and succeeded in reproducing the NXES-like spectra for incident energies **6** and **7**, but those for **8**–**13** could not be reproduced. They interpreted that the NXES-like spectra for **6** and **7** are due to the CT excitation with the $3d^9\underline{L}$ configuration. On the other hand, those for **8**–**13** should be of different origin; probably they are the NXES spectra with the $3d^8\underline{L}$ configuration and an additional electron in the s, p continuum band. The essential reason why the CT excitations **6** and **7** do not have a constant Raman shift but behaves like NXES spectra is that the intermediate state, the CT satellite of the Ni $2p$ XAS, has continuous excited states due to the finite energy width of the O $2p$ valence band. This situation is essentially the same as that where Tanaka et al. [72] predicted theoretically in their old paper (in 1990) on the resonant Ce $5p \rightarrow 3d$ X-ray emission spectra of CeO_2, and Butorin [71] pointed out that this would be the mechanism explaining the behavior of the CT excitation in NiO. More recently Matsubara et al. [73] confirmed it by their careful calculation with SIAM and by comparison with the cluster model calculation. Matsubara et al. [73] showed that the peaks for **6** and **7** are the RIXS spectra due to the CT excitations whose excitation energies 5.8 eV and 8.5 eV correspond to the lowest and highest boundary of the CT excitation continuum. They also calculated the RIXS spectra of NiO by changing the charge transfer energy Δ from 2.0 eV to 6.5 eV by the step of 0.5 eV, and concluded that the most appropriate value of Δ is 3.5 eV. Very recently, Ghiringhelli et al. [74] have succeeded in high resolution RIXS measurements for the d-d excitations of the Ni $2p \rightarrow 3d \rightarrow 2p$ RIXS of NiO, and it is also desirable to perform the high resolution measurements for the CT excitations.

According to Kao et al. [75], the Ni $1s \rightarrow 4p \rightarrow 1s$ RIXS of NiO also exhibits inelastic peaks close to the positions of the two CT excitations mentioned above. Recently Shukla et al. [76] have measured the pressure dependence of the Ni $1s \rightarrow 4p \rightarrow 1s$ RIXS of NiO with the incident energy tuned to the EQ pre-peak of Ni $1s$ XAS. At ambient pressure, they observed two RIXS structures at 5.3 eV and 8.5 eV, corresponding to the CT excitations. With increasing pressure up to 100 GPa, the RIXS intensity decreases and the 5.3 and 8.5 eV structures are smeared out. This is explained by that the width of the CT excitation band increases with the pressure. Since RIXS is a photon-in and photon-out process, it is a powerful tool in the study of electronic states under high pressure [77]. For experimental measurements of the pressure-induced change of electronic structure, such as a high-spin and low-spin phase transition, the $3p \rightarrow 1s$ RIXS (sometimes denoted by $K\beta$ RIXS), as well as $K\beta$ NXES, have been successfully used for various transition metal compounds [78–81].

6 RIXS by electric quadrupole excitation and related phenomena

In the $2p$ core excitation of rare earth systems, the $2p \rightarrow 4f$ electric quadrupole (EQ) excitation is expected to be located on the lower energy side of the strong $2p \rightarrow 5d$ electric dipole (ED) excitation, but by the conventional XAS measurements it is almost invisible because of its weak intensity and large spectral broadening due to the short $2p$ core hole lifetime. The detection of the EQ excitation was enabled by taking advantage of RIXS. Also the RIXS is a powerful tool to detect other hidden structures in XAS.

6.1 Background

A pioneering experiment to detect the EQ excitation was done by Hämäläinen et al. [82], who measured the excitation spectrum of RIXS ($2p \rightarrow 4f$ and $2p \rightarrow 5d$ excitations and $3d \rightarrow 2p$ radiative decay) for Dy compounds with very high spectral resolution. Namely, they measured the change of the L_3-M_5 X-ray emission intensity by changing the incident energy near the threshold of the Dy L_3 XAS, where the emitted X-ray energy is fixed at the fluorescence (so called $L\alpha_1$ XES) peak position corresponding to the energy separation of the $3d_{5/2}$ and $2p_{3/2}$ core levels. They could observe in the excitation spectrum some weak and fine spectral structures in the pre-threshold region of the Dy L_3 edge, and assigned them as the EQ excitation signal. After the experiments, a theoretical analysis for this excitation spectrum was made by Tanaka et al. [83] and Carra et al. [84] They showed that the spectral width of the excitation spectrum is drastically narrowed compared with the conventional XAS, because the former is determined by the $3d$ core-hole lifetime broadening in the final state of RIXS while the latter by the $2p$ one in the final state of XAS. Since then, the structure of the EQ excitation has been studied for various rare earth systems. As an example, Bartolomé et al. [85,86] measured RIXS under the $2p \rightarrow 4f$ excitation and $3d \rightarrow 2p$ radiative decay for various rare earth systems, and found that the EQ excitation of light rare earth systems is split into two peaks. According to their results, the energy separation of the two peaks is almost proportional to the atomic number. Furthermore, they also measured the energy splitting of the EQ excitation in ferromagnetic light rare earth systems by magnetic circular dichroism (MCD) of XAS, and showed that the energy separation measured by RIXS coincides with that by MCD of XAS within the experimental accuracy [85].

6.2 Excitation spectrum of RIXS

More recently new theoretical and experimental developments have been made on the result by Bartolomé et al.

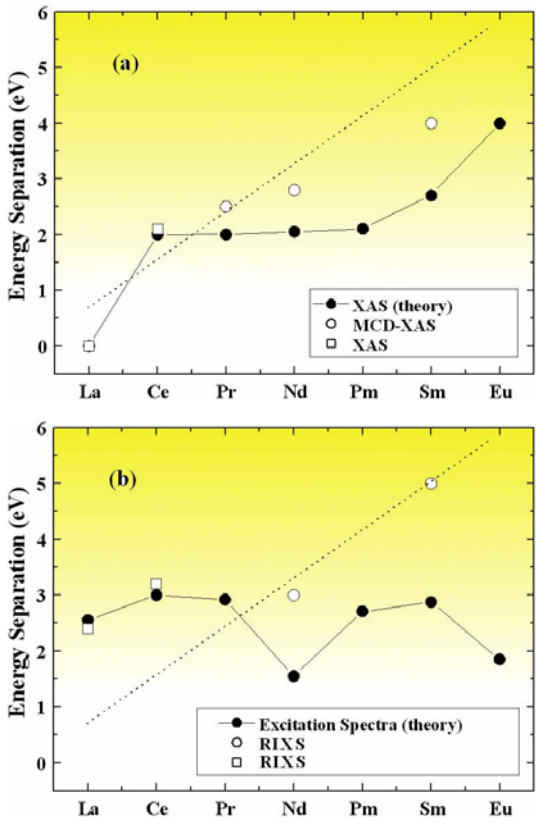

Fig. 16. Calculated energy separation (solid circles) for (a) $2p_{3/2}$-$4f$ XAS and (b) the excitation spectrum of $3d_{5/2}$-$2p_{3/2}$ RIXS under the $2p_{3/2}$-$4f$ excitation. The experimental results of the energy separation are shown with the open circles (from Ref. [85]) and the open squares (from Ref. [87]). The dashed lines are guides for the eye. From Nakazawa et al. [88].

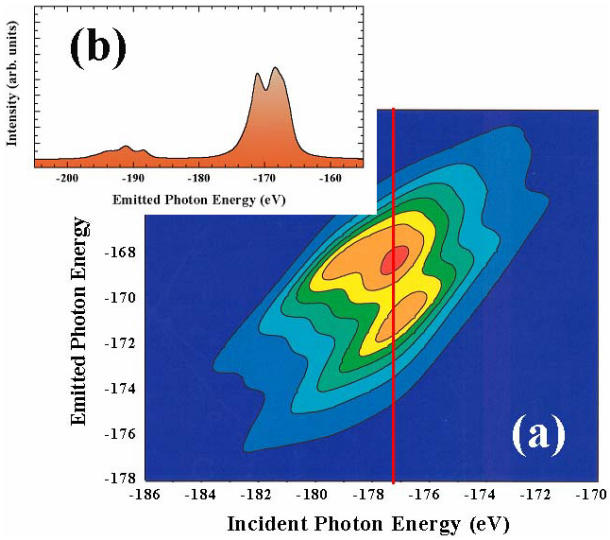

Fig. 17. (a) is the calculated result of RIXS intensity due to the Nd $2p_{3/2}$-$4f$ electric quadrupole excitation and $3d$-$2p_{3/2}$ electric dipole transition in Nd^3+ system, displayed as a contour map in the two-dimension plane spanned by incident and emitted photon energies. In the calculation, the full-multiplet coupling effect is taken into account. (b) is the RIXS spectrum where the incident photon energy is fixed at the vertical line in (a), so that it corresponds to the cross section of the contour map.

Figures 16a and 16b display the energy separation of the EQ excitation peaks in light rare earth elements (from La to Eu) determined by XAS (and MCD-XAS) and RIXS, respectively. The open circles are the results by Bartolomé et al. [85] and the dotted lines are guides for the eye, which indicate that the energy separation of two peaks is roughly proportional to the atomic number. The open squares are new experimental results by Journel et al. [87] for LaF_3 and CeF_3. It is clear that the energy separations given by open squares are not proportional to the atomic number and, furthermore, they are different in XAS and RIXS. Theoretical calculations for these energy separations have been performed by Nakazawa et al. [88] with an atomic model including full multiplet coupling effects. An example of calculated RIXS spectra is shown in Figure 17a for the Nd $2p_{3/2} \rightarrow 4f$ EQ excitation and $3d_{5/2} \rightarrow 2p_{3/2}$ ED transition in Nd^{3+} system, displayed as a contour map in the two-dimension plane spanned by incident and emitted photon energies. The RIXS spectrum is the vertical cross-section of this contour map for a fixed incident photon energy: an example of the RIXS spectrum is depicted in (b) for an incident energy indicated by the vertical line in (a). On the other hand, the excitation spectrum at the fluorescence peak position is the horizontal cross-section of the contour map for the emitted photon energy at –169 eV (which corresponds to $\epsilon_{3d_{5/2}} - \epsilon_{2p_{3/2}}$, but the origin of the photon energy is shifted somewhat arbitrarily).

Here we show why the excitation spectrum of RIXS corresponds to a less broadened version of XAS. Th most essential assumption is that $|j\rangle$ and E_j can be written as

$$|j\rangle = a_{3d_{5/2}} a^{\dagger}_{2p_{3/2}} |i\rangle, \tag{8}$$

$$E_j = \Delta\epsilon + E_i, \tag{9}$$

where $\Delta\epsilon$ is the difference between $3d_{5/2}$ and $2p_{3/2}$ core levels: $\Delta\epsilon = \epsilon_{3d_{5/2}} - \epsilon_{2p_{3/2}}$. This assumption does not necessarily mean that we confined ourselves entirely to the one electron approximation but means that the X-ray emission process occurs simply by the core electron transition between $3d_{5/2}$ and $2p_{3/2}$ states, leaving the other electron states unchanged. We can take into account the many body $4f$-$4f$ and $4f$-$3d$ interactions, but the $4f$-$3d$ interaction ($3d$ core hole effect) is assumed be the same as the $4f$-$2p$ interaction ($2p$ core hole effect).

Substituting equations (8) and (9) into equation (1) and using

$$\omega = \Delta\epsilon, \tag{10}$$

we obtain, apart from an unimportant factor, the expression of the excitation spectrum

$$F(\Omega, \Delta\epsilon) = \sum_i \frac{|\langle i|T_1^{\lambda_1}|g\rangle|^2}{[(\Omega - E_i + E_g)^2 + \Gamma_i^2][(\Omega - E_i + E_g)^2 + \Gamma_j^2]}, \tag{11}$$

where Γ_i and Γ_j are the spectral broadenings by the $2p$ (Γ_L) and $3d$ (Γ_M) core holes. Since Γ_L (~ 2.1 eV) is much larger than Γ_M ($\sim$0.7 eV), we obtain

$$F(\Omega, \Delta\epsilon) \sim I_{\Gamma_M}(\Omega), \tag{12}$$

where $I_{\Gamma_M}(\Omega)$ is the L_3 XAS spectrum with the broadening Γ_L replaced by Γ_M:

$$I_{\Gamma_M}(\Omega) = \sum_i |\langle i|T_1^{\lambda_1}|g\rangle|^2 \frac{\Gamma_M/\pi}{((\Omega - E_i + E_g)^2 + \Gamma_M^2}. \tag{13}$$

The most serious assumption in rare earth materials is equations (8) and (9), so that the expression (13) holds only approximately, as mentioned below.

The results of the energy separation calculated by Nakazawa et al. [88] are shown by closed circles, and found to reproduce well the experimental results by Journel et al., but not to reproduce those by Bartolomé et al. The main points clarified are as follows [88]: (1) The energy separation in XAS is determined by the $4f$-$4f$ interaction. The $4f$-$4f$ exchange interaction causes the energy separation (due to the up and down spin excitation) almost proportional to the atomic number, as mentioned by Bartolomé et al. [85], but the $4f$-$4f$ multipole Coulomb interaction also influences the energy separation, giving rise to considerable modification from the proportionality relation. (2) The energy separation in RIXS is determined not only by the $4f$-$4f$ interaction but also by the $4f$-$3d$ interaction in the final state of RIXS. The situation is very clear in the case of La; since we have no $4f$ electron in the ground state of La, the energy separation vanishes in XAS because of no $4f$-$4f$ interaction, but we have a finite energy separation in RIXS due to the $4f$-$3d$ interaction in the final state.

6.3 Related topics

Precise experimental observations of RIXS spectra in the pre-threshold region (including the EQ excitation) have recently been made for the $1s$ electron excitation of transition metal compounds, Fe compounds, Mn compounds and cuprates. Rueff et al. [89] measured the Fe $2p \rightarrow 1s$ RIXS (sometimes called Fe $K\alpha$ RIXS) following the $1s \rightarrow 3d$ EQ excitation (as well as the $1s \rightarrow 4p$ ED excitation) for a series of four model compounds (minerals) where Fe of valence 2+ or 3+ occupies an octahedral (O_h) or tetrahedral (T_d) site. The common names of samples in mineralogy are andradite, siderite and so on. The experimental results of RIXS spectra in the pre-threshold region are shown as a contour map in the two-dimensional space spanned by Ω and $\Omega - \omega$. Then, by taking the intensity profiles as a function of Ω with fixed values of $\Omega - \omega$ (instead of fixed values of ω) they determined the crystal field level splitting in the $1s \rightarrow 3d$ XAS spectra. For instance, the t_{2g}-e_g splitting in andradite (the case of Fe^{3+} in O_h symmetry) is estimated to be 1.6 eV. Another interesting fact shown in this study is that the RIXS intensity in the pre-threshold region is about a factor of 5 larger when Fe occupies a T_d site than an O_h site. This is reasonable, since the Fe $1s$-$3d$ transition on the O_h site is only allowed for the EQ transition but that on the T_d site is allowed for both EQ and ED transitions due to the lack of inversion symmetry.

Hayashi et al. [90–92] have measured the Cu $2p \rightarrow 1s$ RIXS for CuO, $CuCl_2$ and $Nd_{2-x}Ce_xCuO_4$, and by analyzing the data they obtained the lifetime-broadening-suppressed (or lifetime-broadening-free) version of the Cu $1s$ XAS spectra at the pre-threshold and near-threshold regions due to the Cu $1s \rightarrow 3d$ EQ and $1s \rightarrow 4p$ ED transitions. Their method of analysis is somewhat different from taking the excitation spectrum, but based on a formula connecting the RIXS and XAS spectra, which was first derived by Tulkki and Åberg [93] by one electron approximation. However, the essential approximation (not necessarily limited to the one electron approximation) in their analysis would be easier to understand by starting from equation (1), instead of using the one electron formula by Tulkki and Åberg [93]. By assuming equations (8) and (9), but without using equation (10), equation (1) is written, apart from an unimportant factor, as

$$\begin{aligned} F(\Omega,\omega) &= \sum_i \frac{|\langle i|T_1^{\lambda_1}|g\rangle|^2}{(\Omega - E_i + E_g)^2 + \Gamma_i^2} \\ &\quad \times \frac{1}{(\Omega - \omega - \Delta\epsilon - E_i + E_g)^2 + \Gamma_j^2} \\ &= \int dx \frac{I_0(x)}{[(x-\Omega)^2 + \Gamma_i^2][(\Omega - \omega - \Delta\epsilon - x)^2 + \Gamma_j^2]} \end{aligned} \tag{14}$$

where $I_0(\Omega)$ is the XAS spectrum in the limit of vanishing spectral broadening (see Eq. (13)), and Γ_i and Γ_j are now the spectral broadening due to the lifetime of the $1s$ and $2p$ core holes. It is to be noted that in deriving equation (14) the X-ray emission process from $|i\rangle$ to $|j\rangle$ is assumed to be a one electron transition between core levels, leaving all the other electronic states unchanged, but any other many body effects can be included.

What Hayashi et al. did is to select a few values of the incident energy Ω and to determine the functional form of $I_0(\Omega)$ so as to reproduce the experimental RIXS spectra $F(\Omega,\omega)$ through equation (14) for all sets of Ω. The numerical calculations were made by trial and error method, starting from an appropriate functional form of $I_0(\Omega)$. They obtained the spectrum $I_0(\Omega)$ (or that broadened by Γ_j) for various Cu compounds in the region of $1s \rightarrow 3d$ EQ and $1s \rightarrow 4p$ ED transitions. It is to be remarked that the obtained $I_0(\Omega)$ is not necessarily a simple one electron excitation spectrum but also includes many-body structures, for instance the charge transfer structures induced by the attractive core hole potential acting on the Cu $3d$ states. On the other hand, the validity of the simple assumption of the one electron transition in the X-ray emission process should be checked carefully.

Hayashi et al. [94,95] also measured the Mn $3p \rightarrow 1s$ RIXS (sometimes called $K\beta$ RIXS) for Mn compounds, MnO, Mn_2O_3, MnO_2 and $KMnO_4$, and analyzed the spin-polarized ED and EQ excitation spectra by applying their

method but extending $I_0(\Omega)$ as spin-dependent functions. It is also to be mentioned that the Mn $K\beta$ RIXS spectra for MnF_2 and MnO by the Mn $1s \rightarrow 3d$ EQ excitation have been studied in detail by Taguchi et al. [96] and Shoji et al. [97], respectively.

We now switch the topics to RIXS of rare earth systems. Hayashi et al. [98] measured the Dy $3d_{3/2,5/2} \rightarrow 2p_{3/2}$ RIXS (sometimes called Dy $L\alpha_1$ RIXS) spectra of Dy metal, and tried to obtain the lifetime-broadening-suppressed Dy L_3 XAS in the EQ transition region by applying their method of spectral analysis. In order to take into account the multiplet coupling effect between $3d$ and $4f$ states in the final state of RIXS, they introduced a "final state density function". However, as shown by Nakazawa et al. [88], it is difficult to separate multiplet coupling effects in the intermediate and final states of RIXS. This is because the transition matrix element $\langle j|T_2^{\lambda_2}|i\rangle$ of the X-ray emission process depends on both $|i\rangle$ and $|j\rangle$, and hence the final state density function cannot be factorized as they assumed. It should be examined carefully whether the experimental contour map of RIXS intensity (in the Ω and ω space) of the EQ transition region (something like Fig. 17) can be well reproduced by their method of analysis. Also a more detailed study would be needed to check whether the EQ transition signals in XAS (as a function of Ω) and in RIXS (as a function of ω) have some multiplet structures, instead of their results of a simple single peak structure.

The RIXS technique is a powerful means to reveal hidden structures in XAS spectra, not only the EQ signal but also some hidden ED signals. The Ce L_3 XAS spectra of tri-valence and mixed valence Ce compounds exhibit single-peak (corresponding to the $4f^1$ final state) and double-peak ($4f^0$ and $4f^1$ final states) structures, respectively, but the $4f^2$ contribution cannot be detected by the conventional XAS measurements, because of its small intensity and the large spectral width due to the lifetime broadening of the $2p$ core hole. On the other hand, if one measure the Ce $3d \rightarrow 2p$ RIXS with the incident energy tuned appropriately on the lower energy side of the main Ce L_3 XAS peak, it is possible to detect the signal of the $4f^2$ final state in the RIXS spectrum, where the spectral width is reduced to the lifetime broadening of the $3d$ core hole. Rueff et al. [99] measured the Ce $3d_{5/2} \rightarrow 2p_{3/2}$ RIXS spectra for Ce-Th and Ce-Sc alloys which show the γ-α transition at finite temperature (see also [53]). They analyzed their data and derived the f^1/f^2 intensity ratio in the Ce L_3 XAS by changing the temperature. The temperature variation of the f^1/f^2 intensity ratio shows a sharp drop across the γ-α transition and hysteresis, which closely resemble the magnetization loop. Rueff et al. claim that these measurements confirm recent dynamical mean-field calculations [100,101] that predict significant f^2 occupancy in the ground state. This finding is very interesting, but one should be careful in that the f^1/f^2 intensity ratio observed experimentally is not in the ground state quantity but in the intermediate state of RIXS (the final state of XAS). It is not very clear at present what is the relationship of the f^1/f^2 intensity ratios in the ground and core excited states.

In addition to Ce compounds, Yb compounds often behave as mixed valence materials or heavy Fermion systems. Here, the Yb $4f^{13}$ (Yb^{3+}) and $4f^{14}$ (Yb^{2+}) configurations are mixed in the ground states, instead of the Ce $4f^0$ (Ce^{4+}) and $4f^1$ (Ce^{3+}) configurations in Ce compounds. Dallera et al. [102] observed the valence change of $YbInCu_4$ and $YbAgCu_4$ as a function of temperature by measuring the excitation spectra of the Yb $L\alpha_1$ RIXS (they call this "XAS in the partial fluorescence yield mode"). The valence change in Yb compounds had been measured by photoemission spectroscopy (PES), but since the PES spectra are surface-sensitive, the interpretation of the results was controversial. The experiments by Dallera et al. detect the unambiguous bulk behavior of the Yb valence change and solved the problem. It is shown that the valence change in $YbInCu_4$ occurs suddenly at a phase transition temperature, while that in $YbAgCu_4$ occurs continuously in a consistent manner with the prediction of SIAM (Kondo temperature of 70 K). Dallera et al. [103] also measured the valence change of the mixed valence compound $YbAl_2$ under external pressure. They found that the Yb valence number increases from 2.25 at ambient pressure to 2.9 at 385 Kbar. These measurements demonstrate clearly that RIXS is a new powerful tool to probe the bulk electronic configuration in strongly correlated systems.

7 Magnetic circular dichroism in RIXS of ferromagnetic systems

7.1 Longitudinal and transverse geometries in MCD-RIXS

Let us consider the situation shown in Figure 18. The magnetization of a ferromagnetic thin-film sample is parallel to the sample surface and the angle between the incident X-ray (emitted X-ray) and the magnetization is θ_1 (θ_2). The MCD in RIXS (denoted by MCD-RIXS) spectrum is defined by the difference of RIXS spectra for incident photons with $-$ and $+$ helicities, where the helicity of the emitted photon is not detected (see also the paper by Duda [104]).

Before giving some expressions of MCD-RIXS, we decompose the expression (1) of RIXS spectrum as follows:

$$F(\Omega,\omega) = \left\{ \sum_{j,i} \left| \frac{\langle j|T_2^{\lambda_2}|i\rangle\langle i|T_1^{\lambda_1}|g\rangle}{E_g+\Omega-E_i+i\Gamma_i} \right|^2 + \sum_{j,i,i'} \left[\frac{\langle j|T_2^{\lambda_2}|i\rangle\langle i|T_1^{\lambda_1}|g\rangle \left(\langle j|T_2^{\lambda_2}|i'\rangle\langle i'|T_1^{\lambda_1}|g\rangle\right)^*}{(E_g+\Omega-E_i+i\Gamma_i)(E_g+\Omega-E_{i'}-i\Gamma_{i'})} + \text{c.c.} \right] \right\} \frac{\Gamma_j/\pi}{(E_g+\Omega-E_j-\omega)^2+\Gamma_j^2}, \quad (15)$$

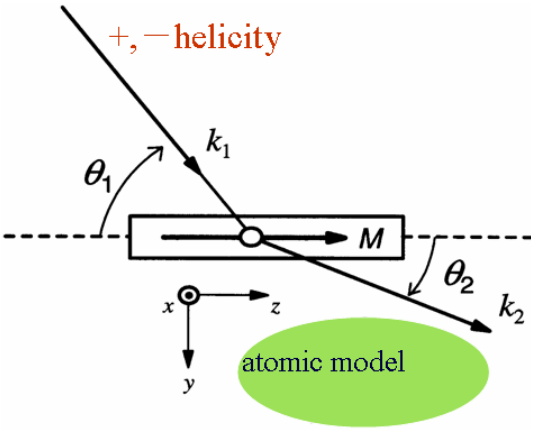

Fig. 18. Geometrical alignment of MCD-RIXS.

where the first and the second terms in the curly bracket of equation (15) are the diagonal and cross terms in the expansion of $|\ldots|^2$ in equation (1). The diagonal term represents the two-step process of RIXS, where the whole process is described by two successive processes, X-ray absorption and X-ray emission. On the other hand, the cross term describes the RIXS process from the ground state to the final state via different intermediate states which interfere each other. Therefore, the cross term is denoted by the interference term.

By the definition mentioned above, the spectrum of MCD-RIXS $\Delta F(\Omega,\omega)$ is given by

$$\Delta F(\Omega,\omega) \equiv \sum_{\lambda_2} \left\{ [F(\Omega,\omega)]_{(\lambda_1=-)} - [F(\Omega,\omega)]_{(\lambda_1=+)} \right\}. \tag{16}$$

With the atomic model, we can calculate analytically the dependence of MCD-RIXS on θ_1 and θ_2. By assuming the ED transition both for excitation and de-excitation processes, we obtain, from the group theoretical consideration, the analytic expression of MCD-RIXS in the following form [105,106]:

$$\Delta F(\Omega,\omega) = \sum_f \left\{ -\frac{1}{2}\cos\theta_1 \left[(1+\cos^2\theta_2)F_1 + 2\sin^2\theta_2 F_2 \right] - \frac{1}{4}(\sin\theta_1 \sin 2\theta_2)F_3 \right\} \times \frac{\Gamma_f/\pi}{(E_g+\Omega-E_f-\omega)^2+\Gamma_f^2}, \tag{17}$$

where F_1, F_2 and F_3 are factors independent of θ_1 and θ_2. The present calculation is valid not only in the atomic model but also in more general models (for instance in SIAM) with SO_3 symmetry.

This result indicates a remarkable fact: In the curly bracket of (17), the first and second terms, which are proportional to $\cos\theta_1$ and $\sin\theta_1$, originate from the diagonal term and interference term contributions, respectively. Therefore, when the incident X-ray direction is parallel to the magnetization (denoted by the longitudinal geometry (LG)), we have only the diagonal term contribution, while

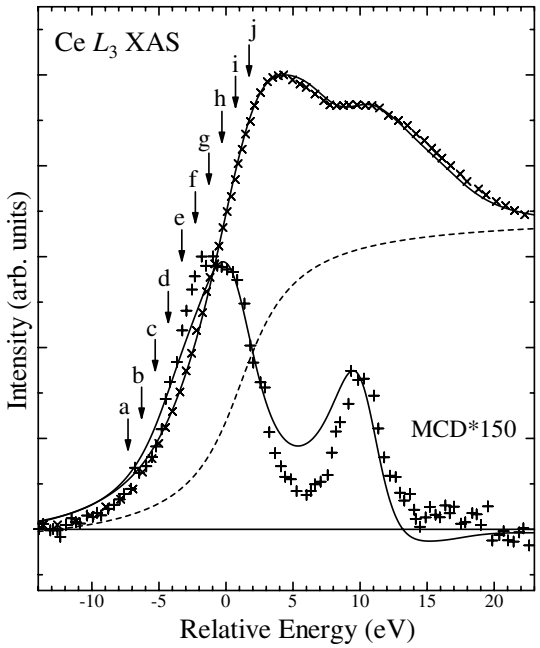

Fig. 19. Calculated results (solid curves) and the experimental ones (crosses) of XAS and MCD-XAS at the L_3 edge of $CeFe_2$. The dashed curve represents the background contribution taken in the calculation. From Asakura et al. [111].

for the incident X-ray perpendicular to the magnetization (denoted by the transverse geometry (TG)), we have only the interference term contribution. For arbitrary value of θ_1 between 0° and 90°, MCD-RIXS is given by a superposition of the diagonal and interference terms, but it has been checked that the diagonal term contribution is dominant except for θ_1 very close to 90°. Another remarkable fact is that in TG the θ_2 dependence of MCD-RIXS is given simply by $\sin 2\theta_2$. On the other hand, the θ_2 dependence of MCD-RIXS in LG is much smaller. Similar calculations can also be made for the case where the X-ray excitation is due to the EQ transition and the X-ray de-excitation due to the ED transition [109].

Here we have considered the simple geometrical alignment shown in Figure 18. For more general cases where the directions of the incident and emitted X-rays are described by (θ_1,ϕ_1) and (θ_2, ϕ_2), the angle dependence of MCD-RIXS has been given by Ogasawara et al. [107] and Ferriani et al. [108].

7.2 Application of MCD-RIXS in LG to detecting Ce $4f^2$ contribution in mixed-valence ferromagnetic compound $CeFe_2$

In this section we give a theoretical prediction to apply MCD-RIXS in LG to detecting hidden structures in MCD-XAS. As an example, we discuss the hidden $4f^2$ contribution in the Ce L_3 MCD-XAS of mixed valence ferromagnetic compound $CeFe_2$.

The calculations of XAS, MCD-XAS, RIXS and MCD-RIXS were made by Asakura et al. [110,111] In Figure 19,

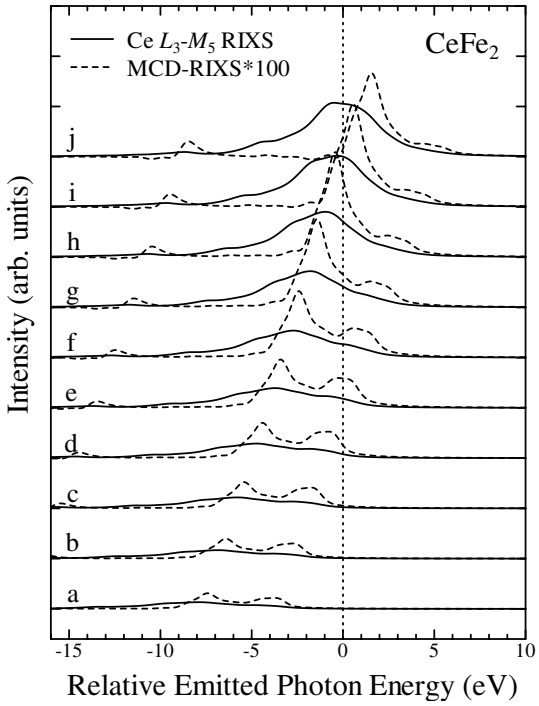

Fig. 20. Calculated results of the Ce L_3-M_5 RIXS (solid curves) and MCD-RIXS (dashed curves) for $CeFe_2$. The incident X-ray energies are taken at the positions **a-j** shown in Figure 19. From Asakura et al. [111].

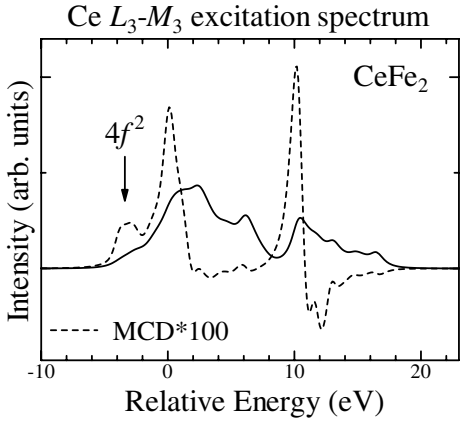

Fig. 21. Calculated results of excitation spectra of the Ce L_3-M_5 RIXS (solid curve) and its MCD (dashed curve) for $CeFe_2$. From Asakura et al. [111].

we show the calculated results (solid curves) of the Ce L_3 XAS and its MCD, compared with the experimental results (cross marks) by Giorgetti et al. [112] In order to calculate the conduction band state of $CeFe_2$, which consists of the Ce 5d and Fe 3d states, they used the LCAO method with the $Ce_{35}Fe_{76}$ cluster model. On the other hand, in order to describe the mixed valence character of the Ce 4f state they used SIAM. The dashed curve is the background contribution assumed in this calculation, and the spectral broadening Γ_m (mainly due to the 2p core hole lifetime) is taken as 3.0 eV so as to reproduce the spectral broadening of the experimental data. The agreement between the calculated and experimental results is good.

Both of the XAS and MCD-XAS spectra exhibit the double-peak structure: the higher energy peak of XAS (and MCD-XAS) corresponds mainly to the Ce $4f^0$ configuration and the lower energy one to the Ce $4f^1$ and $4f^2$ configurations. The contributions from the Ce $4f^1$ and $4f^2$ configurations cannot be observed separately because the spectral broadening by Γ_m is very large and the intensity of the $4f^2$ contribution is smaller than that of the $4f^1$. It can be shown that RIXS (especially MCD-RIXS in LD) is a powerful tool to detect the hidden $4f^2$ contribution. In Figure 20, we show the calculated Ce L_3-M_5 ($3d_{5/2} \rightarrow 2p_{3/2}$) RIXS (solid curves) and its MCD-RIXS (dashed curves) as a function of the emitted photon energy whose origin is taken at the energy difference of the Ce $3d_{5/2}$ and $2p_{3/2}$ core levels. The angles θ_1 and θ_2 are taken to be 0° and 54.7°, respectively. The incident photon energy is tuned at the positions **a** to **j** shown in Figure 19, and the effect of the background contribution in XAS is disregarded for simplicity. The spectral broadening Γ_f is taken as 0.7 eV, which corresponds to the lifetime broadening of the Ce 3d core hole. In the region of **a** to **j**, the RIXS (especially MCD-RIXS) spectra exhibit a double peak structure, consisting of the Ce $4f^2$ (higher energy peak) and $4f^1$ (lower energy one) contributions, which can be separated due to the spectral broading Γ_f smaller than Γ_m.

In order to get a less broadened version of the MCD-XAS (XAS), we should take the excitation spectrum of MCD-RIXS (RIXS). We show in Figure 21 the excitation spectra of the L_3-M_5 RIXS and its MCD-RIXS with the emitted photon energy fixed at the energy difference of the Ce $3d_{5/2}$ and $2p_{3/2}$ core levels. Namely, the amplitudes of the L_3-M_5 RIXS and its MCD-RIXS just along the dotted line in Figure 20 are shown in Figure 21. Here we can see clearly the $4f^2$ contribution (indicated by an arrow) especially in the excitation spectrum of MCD-RIXS (dashed curve). It can be shown, furthermore, that if we reduce the value of Γ_m in the calculation of Figure 19 from 3.0 eV to 0.7 eV the calculated results agree almost perfectly with Figure 21. In Section 6.2, we have discussed that the excitation spectrum of the rare earth L_3-M_5 RIXS is different from the less broadened version of L_3 XAS mainly because of the $4f$-3d interaction in the final state of RIXS. In $CeFe_2$, however, the Ce $4f$ state is almost in the spin singlet and orbital singlet state, so that the $4f$-3d interaction can be disregarded.

We have shown theoretically that the technique of the excitation spectrum of MCD-RIXS is very useful to observe fine structures of MCD-XAS beyond the lifetime broadening of the L_3 core hole. This technique is an extension of the technique of the excitation spectrum of RIXS by Hämäläinen et al. [82] to MCD-RIXS. It is highly desirable that the present theoretical prediction of observing the Ce $4f^2$ signal by the excitation spectrum of MCD-RIXS will be confirmed by experimental observations, and that the present technique will be used more generally in order to get the high resolution MCD spectra.

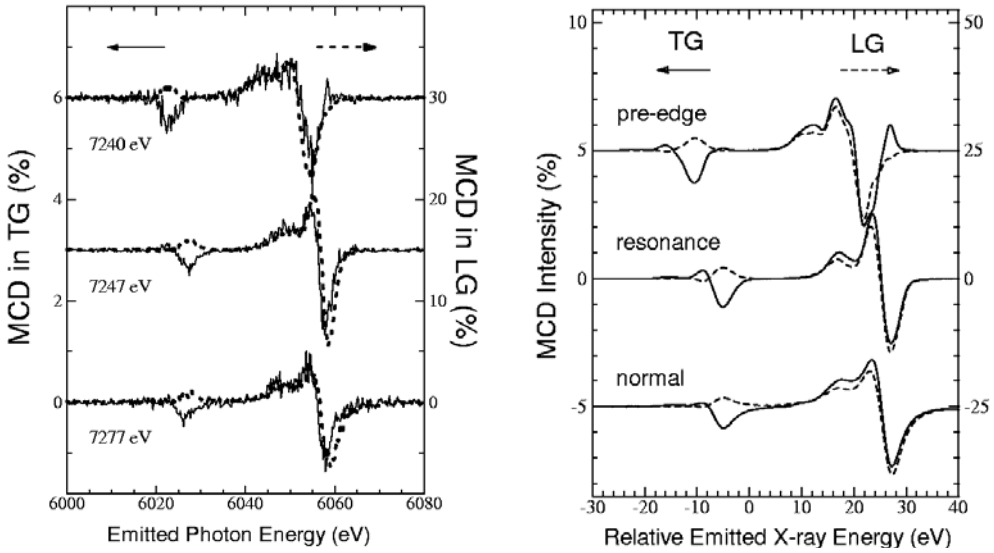

Fig. 22. (a) Experimental and (b) theoretical results of the Gd L_3-$M_{4,5}$ MCD-RIXS for incident X-ray energies at the pre-edge (7240 eV), resonance (7247 eV) and normal (7277 eV) excitations. The results TG and LG are shown with the solid and dashed curves, respectively. From Fukui et al. [106].

7.3 Experimental and theoretical studies of MCD-RIXS in TG

MCD-RIXS in TG was first observed experimentally by Braicovich et al. [113] for $2p \rightarrow 3d$ excitation and $3s \rightarrow 2p$ de-excitation in $NiFe_2O_4$ and Co metal (see also [68]). They observed non-vanishing MCD-RIXS and explained this as being an effect of the polarization of the core hole [114]. They did not report the details of the spectral analysis. After that, Fukui et al. [105,106] measured non-vanishing MCD-RIXS for the Gd L_3 excitation and Gd $3d \rightarrow 2p_{3/2}$ de-excitation (i.e., L_3-$M_{4,5}$ MCD-RIXS) of $Gd_{33}Co_{67}$ amorphous alloy. They made a theoretical analysis with an atomic model for Gd^{3+}, and showed that MCD-RIXS in TG is caused by the interference process in the coherent second-order optical process, while that in LG consists of two successive real processes, as mentioned in Section 7.1.

The results of measured Gd L_3-$M_{4,5}$ MCD-RIXS spectra are shown in Figure 22a, where the incident X-ray energy is taken at three different values, 7240 eV (pre-threshold region), 7247 eV (main peak resonance), and 7277 eV (high energy continuum for normal fluorescence), and the MCD-RIXS spectra are shown with the solid curves for TG and the dashed curves for LG. Here the angle θ_2 is fixed at 45°. The strong MCD-RIXS in the higher emitted X-ray energy corresponds to the contribution from the $3d_{5/2}$ state, while the weak one in the lower energy to the contribution from the $3d_{3/2}$ state. The spectral shape in TG is similar to that in LG for the $3d_{5/2}$ contribution, while the sign of TG is opposite to that of LG for the $3d_{3/2}$ contribution. It is to be noted that the scale of the MCD-RIXS intensity in Figure 22a is different for TG and LG, and it is found that the amplitude of the MCD-RIXS in TG is about one fifth of that in the LG.

The calculated results corresponding to the experimental data are shown in Figure 22b. The calculated and experimental results are in good agreement with each other both in the spectral shape and the spectral intensity ratio in TG and LG. Furthermore, the θ_2 dependence of MCD-RIXS spectra in the transverse geometry has also been measured with the incident X-ray energy at 7247 eV, and it is confirmed that the dependence is well described by $\sin 2\theta_2$ as given by the theoretical calculation. The result is shown in Figure 23, where A(•), B(+) and C(∘) are intensities of an MCD-RIXS peak by the $3d_{3/2} \rightarrow 2p_{3/2}$ transition, and of two MCD-RIXS peaks by the $3d_{5/2} \rightarrow 2p_{3/2}$ transition, respectively, and they are displayed as a function of the angle θ_2 (actually, as a function of the scattering angle θ_2+90°). The theoretical result is shown with the solid curves, and is found to be in reasonable agreement with the experimental result. This is the evidence that almost pure interference contribution has been observed in MCD-RIXS experiments in TG.

Another interesting challenge of experimental observations will be to detect MCD-RIXS by EQ excitation. Recently Nakamura et al. [115] succeeded in measuring the MCD-RIXS of Sm-Co amorphous alloy by Sm $L_{2,3}$-$N_{4,5}$ EQ excitation and Sm $M_{4,5}$-$L_{2,3}$ ED radiative decay, but the measurements were made for angles θ_1 and θ_2 fixed at 36.9° and –35.3°, respectively, where the contribution of LG is predominant.

More recently, Fukui and Kotani [109] have made the calculation for more general values of θ_1 and θ_2, and predicted theoretically what is expected for MCD-RIXS for EQ and ED excitations of the Sm system. Some examples are shown in Figure 24, where the EQ and EQ+ED contributions are shown with the dashed and solid curves, respectively, and the incident X-ray energy is fixed at the EQ excitation energy determined by the MCD-XAS

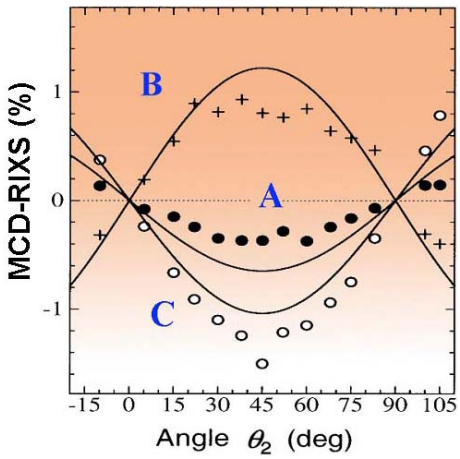

Fig. 23. Experimental result of θ_2 dependence of MCD-RIXS in the transverse geometry for three different emitted photon energies A (closed circle), B (cross) and C (open circle). The solid curves are the calculated ones. From Fukui et al. [106].

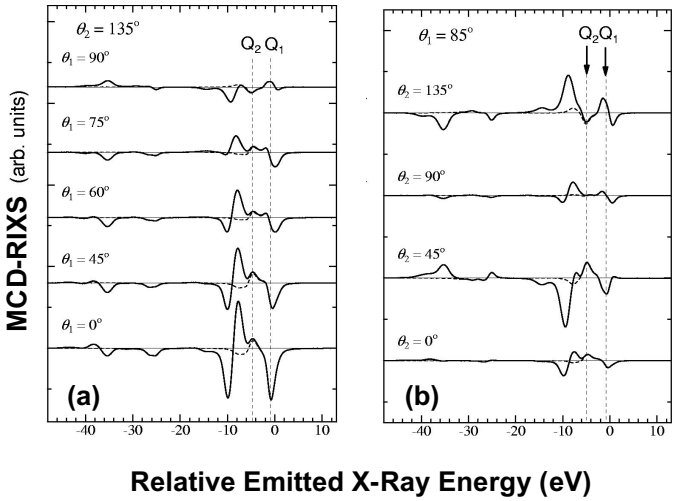

Fig. 24. Calculated results of (a) incident angle dependence and (b) emitted angle dependence of MCD-RIXS for Sm^{3+} system. From Fukui and Kotani [109].

spectrum, but the ED excitation also occurs at the same time. The features Q_1 and Q_2 originate from the EQ excitation. In Figure 24a, the value of θ_1 is fixed at 135° and the value of θ_2 is changed. For $\theta_1 = 0°$ and 45°, the spectral shape is almost the same with only the change in the amplitude, and this means that in this range of θ_1 the diagonal term contribution is dominant. For $\theta_1 = 60°$, the spectral shape changes slightly, and for $\theta_1 = 75°$ it changes considerably by the contribution of the interference term. For $\theta_1 = 90°$, the spectral shape changes drastically, where the interference term gives the 100% contribution. It is interesting to see that for the pure interference term the ED contribution vanishes in the energy region of Q_2, so that for $\theta_1 = 90°$ we can extract the pure EQ contributions Q_1 and Q_2 separately from the ED contribution.

In Figure 24b, we show the change of the MCD-RIXS spectral shape with the change of θ_2. The value of θ_1 is fixed at 85°, because the spectral shape depends strongly on θ_2 only for θ_1 close to 90°, where the interference term gives important contribution. The spectral shape of Q_1 and Q_2 changes in a complicated way with the change of θ_2, reflecting that the angle dependence of the interference term of the EQ contribution is very complicated. Especially for $\theta_2 = 90°$ in Figure 24b, Q_1 does not exhibit a peak but a dispersive spectral shape, and furthermore, the spectral intensity in the Q_2 region almost vanishes.

Experimental study on the angle dependence of MCD-RIXS by the EQ excitation, including the case of TG, and comparison with theoretical results will be desirable in future investigations.

Finally, we would like to discuss the sum rule of MCD-RIXS, which is an important application of MCD-RIXS in TG. Since the RIXS is the second order optical process, it is necessary, for the derivation of the sum rule, to take approximately out the resonance denominator ($E_g + \Omega - E_i + i\Gamma_i$ in Eq. (1)) from the summation over i. This approximation is called "fast collision approximation" [116], which implies that Γ_i (assumed to be independent of i) is much larger than the energy separation of different multiplet terms that interfere in the RIXS process. Then the MCD-RIXS intensity integrated over both Ω and ω (denoted by integrated MCD-RIXS) is related with the multipole moments of physical quantities, charge, angular momentum and so on, in the ground state. Therefore, from the angular dependence of the integrated MCD-RIXS, one can estimate the ground state multipole moments.

First experimental observations of the integrated MCD-RIXS in TG have recently been made by Braicovich et al. [117] for Co $2p \rightarrow 3d$ excitation and $3s \rightarrow 2p$ deexcitation of $CoFe_2O_4$. The angle between the incident and emitted X-rays is fixed at a finite value, but the emitted X-ray direction is changed with the incident direction as an axis of rotation. Here, both excitation and deexcitation processes are due to the ED transition, and then the integrated MCD-RIXS is related with the first order (dipole) and third order (octupole) moments of ground state quantities. The angular dependence of the integrated MCD-RIXS is given, essentially the same manner as that of the MCD in resonant photoemission [118], in terms of ground state multipole moments. Braicovich et al. obtained the ground state moments of Co $3d$ holes up to fourth order by combining the measurements of MCD-RIXS with the sum of + and − helicities in RIXS, and linear and circular dichroism in XAS. The obtained moments are compared with those calculated with the atomic model and the cluster model, and discussed the quenching of these moments in solid state. Van der Laan et al. [119] have made a similar analysis of ground state moments for $CoFe_2O_4$ and $NiFe_2O_4$. The obtained dipole, quadrupole and octupole moments of the $3d$ hole charge in Co and Ni are compared with those calculated with atomic and cluster models. The difference in the quenching of these moments for Co and Ni ferrites is recognized, and the trend is rather consistent with the cluster model calculation.

It is to be noted that the above-mentioned approach toward the sum rule of MCD-RIXS is still in the test case, and further development is expected in future. The applicability of the fast collision approximation should be examined more carefully in order to obtain the more quantitative and accurate results, but the consistency of the obtained results with the cluster model calculation is encouraging. Furthermore, beyond the sum rule of MCD-RIXS, the information on the electronic and magnetic properties of photo-excited states will be the topics expected in future investigations of MCD-RIXS.

8 Concluding remarks

The development of the RIXS study for these 4–5 years is remarkable due to the exploitation of high brilliance synchrotron radiation sources. RIXS is one of the most powerful tools available for the study of electronic states in solids. In contrast to the photoemission spectroscopy (PES), which has been widely used for the study of electronic states, RIXS has a clear advantage that it is a bulk-sensitive and site-selective probe. Furthermore, the information brought by RIXS is complementary to PES; RIXS detects the charge-neutral excitation (electron-hole pair excitation), while PES detects the charged excitation (hole excitation). We should stress that RIXS is a photon-in and photon-out process, so that this technique can be performed in applied electric field or magnetic field or high pressure, as well as it is equally applicable to metals and insulators. Since RIXS is the coherent second order optical process, the information brought by RIXS includes both X-ray absorption process (information by XAS) and X-ray emission process. Furthermore, RIXS can provide us the information originating from the interference of the X-ray absorption and X-ray emission processes, characteristic of the coherent second order spectroscopy.

The core-level spectroscopies, XAS and XPS, accompany intrinsic spectral broadening inherent in the lifetime of the core hole, so that we have a limitation in the spectral width even with extremely high instrumental resolution. In contrast, the quality of RIXS can be improved unlimitedly by improving the instrumental resolution. We have shown in Section 6 that the RIXS can detect hidden structures in the conventional XAS. Furthermore, the intrinsic spectral broadening of elementary excitations detected, for instance, by $1s \rightarrow 4p \rightarrow 1s$ or $2p \rightarrow 3d \rightarrow 2p$ RIXS of transition metal elements, becomes smaller and smaller with decreasing the excitation energy. Therefore, the improvement in the instrumental resolution is one of the most important technical subject in the developments of RIXS in the near future. For instance, the accuracy of the observation of the momentum dependence of charge transfer excitations in cuprates strongly depends on the instrumental resolution. The measurements of the collective orbital excitation (orbiton) in orbital ordered perovskite manganites, as well as the gap excitations in spin-density wave, charge density wave and superconducting states in various materials, would become possible in future. Moreover, most of these gap excitations are expected to be sensitive to the applied magnetic field and pressure, so that RIXS should be the unique technique for these measurements.

The other interesting aspects in future developments of RIXS would be the magnetic circular dichroism in RIXS and the interference effect of the X-ray absorption and X-ray emission processes in RIXS, as discussed in Section 7. The signal of the MCD-RIXS is weaker than that of the conventional RIXS, so that the precise measurements of MCD-RIXS are not easy at present. For instance, the measurements of excitation spectra of MCD-RIXS in $CeFe_2$ would be very difficult because of the weak intensity. We have to wait for X-ray sources with higher brightness. The study of MCD-RIXS in TG and its sum rule will also be much developed, both experimentally and theoretically, as a fertile field of RIXS in future.

The time resolved RIXS measurements would be a promising subject in the future investigations; when the incident X-ray is given by a short pulse, the time response of the X-ray emission reflects the dynamics of the electronic excitations. With the synchrotron radiation sources, the observable time response is too slow to be detected within the core-hole lifetime, but the advent of X-ray Laser (free electron Laser) sources expected in future will make the quick time response of RIXS measurements possible.

Finally, a few words are given for the theoretical study in RIXS. In the present paper, the theoretical calculations are made mainly with SIAM or cluster model including a single cation (transition metal ion), and only some calculations are made with cluster models including several number of cations. In order to calculate the momentum dependence of elementary excitations in more details, the model describing the effect of the translational symmetry of atomic arrangement will be required. For strongly correlated electron systems, the most reliable calculation of RIXS is based on the direct diagonalization method of Hamiltonian for finite systems, but a serious problem is the limit in the system size for the direct diagonalization method. Some appropriate approximation methods to treat the correlation effect for RIXS in infinite systems would be the important subject to be solved. Most calculations for RIXS in d and f electron systems have so far based on some model calculations such as SIAM and cluster models, but the role of ab initio calculations will become more and more important. Also, an appropriate combination of ab initio and model calculations would be a promising theoretical approach in future.

The author would like to thank Drs. S. Shin, H. Maruyama, K. Okada, I. Harada, S. Tanaka, H. Ogasawara, T. Uozumi, M. Nakazawa, M. Taguchi, T. Idé, M. Matsubara, K. Fukui, K. Asakura, T. Iwazumi, T. Nakamura, H. Shoji, S. Nanao, Y. Harada, T. Kinugasa, R. Eguchi, J. C. Parlebas, F. M. F. de Groot, J. Nordgren, S. M. Butorin, L. C. Duda, M. Magnuson, T. Schmitt, J.-H. Guo, C. Hague, J.-M. Mariot, L. Braicovich, G. Ghiringhelli, C. Dallera, J. P. Hill, C.-C. Kao, K. Hämäläinen, A. Shukla, M. Calandra, J.-P. Rueff, D. Chandesris and P. Le Fèvre for collaborations and discussions. This paper is partially supported by the JSPS-CNRS

Cooperation Program on "Electronic properties of correlated materials: High resolution resonant inelastic X-ray scattering". The finish of this paper has been made during the author stays temporarily in Laboratoire de Minéralogie-Cristallographie de Paris, and he would like to thank Drs. A. Shukla and M. Calandra for their hospitality.

References

1. See, for instance, *Soft X-Ray Emission Spectroscopy*, edited by J. Nordgren, E.Z. Krumaev, J. Electron Spectrosc. Relat. Phenom. (special issue) **110-111** (2000)
2. See, for instance, A. Kotani, S. Shin, Rev. Mod. Phys. **73**, 203 (2001)
3. P. Glatzel, U. Bergmann, Coord. Chem. Rev. **249**, 65 (2005)
4. H.H. Kramers, W. Heisenberg, Z. Phys. **31**, 681 (1925)
5. A. Kotani, in *Theory and Computation for Synchrotron Radiation Spectroscopy*, edited by M. Benfatto, C.R. Natori, E. Pace (AIP, 2000), p. 13
6. A. Kotani, J. Electron Spectrosc. Relat. Phenom. **110-111**, 197 (2000)
7. A. Kotani, J. Synchrotron Rad. **8**, 110 (2001)
8. A. Kotani, in *X-Ray and Inner-Shell Processes*, edited by A. Bianconi, A. Marcelli, N.L. Saini (AIP, 2003), p. 338
9. A. Kotani, J. Electron Spectrosc. Relat. Phenom. **137-140**, 669 (2004)
10. See, for instance, O. Gunnarsson, K. Schönhammer, Phys. Rev. B **28**, 4315 (1983)
11. S. Tanaka, A. Kotani, J. Phys. Soc. Jpn. **62**, 464 (1993)
12. L.C. Duda, Ph.D. thesis, Uppsara University, 1996
13. L.C. Duda, G. Dräger, S. Tanaka, A. Kotani, J. Guo, D. Heumann, S. Butorin, N. Wassdahl, J. Nordgren, J. Phys. Soc. Jpn. **67**, 416 (1998)
14. L.-C. Duda, J. Nordgren, G. Dräger, S. Bocharov, Th. Kirchner, J. Electron Spectrosc. Relat. Phenom. **110-111**, 275 (2000)
15. P. Kuiper, J.-H. Guo, C. Såthe, L.-C. Duda, J. Nordgren, J.J. Pothuizen, F.M.F. de Groot, G.A. Sawatzky, Phys. Rev. Lett. **80**, 5204 (1998)
16. J.P. Hill, C.C. Kao, W.A.C. Caliebe, M. Matsubara, A. Kotani, J.L. Peng, R.L. Greene, Phys. Rev. Lett. **80**, 4967 (1998)
17. T. Idé, A. Kotani, J. Phys. Soc. Jpn. **68**, 3100 (1999)
18. F.C. Zhang, T.M. Rice, Phys. Rev. B **37**, 3759 (1988)
19. G. Ghiringhelli, N.B. Brookes, E. Annese, H. Berger, C. Dallera, M. Grioni, L. Perfetti, A. Tagliaferri, L. Braicovich, Phys. Rev. Lett. **92**, 117406 (2004)
20. M.Z. Hasan, E.D. Isacs, Z.-X. Shen, L.L. Miller, K. Tsutsui, T. Tohyama, S. Maekawa, Science **288**, 1811 (2000)
21. P. Wróbel, R. Eder, Phys. Rev. B **66**, 35111 (2002)
22. M.Z. Hasan, P.A. Montano, E.D. Isacs, Z.-X. Shen, H. Eisaki, S.K. Sinha, Z. Islam, N. Motoyama, S. Uchida, Phys. Rev. Lett. **88**, 177403 (2002)
23. K. Tsutsui, T. Tohyama, S. Maekawa, Phys. Rev. Lett. **83**, 3705 (1999)
24. K. Tsutsui, T. Tohyama, S. Maekawa, Phys. Rev. B **61**, 7180 (2000)
25. C. Kim, A.Y. Matsuura, Z.-X. Shen, N. Motoyama, H. Eisaki, S. Uchida, T. Tohyama, S. Maekawa, Phys. Rev. Lett. **77**, 4054 (1996)
26. T. Nomura, J. Igarashi, J. Phys. Soc. Jpn. **73**, 1677 (2004)
27. Y.J. Kim, J.P. Hill, C.A. Burns, S. Wakimoto, R.J. Birgeneau, D. Casa, C.T. Venkataraman, Phys. Rev. Lett. **89**, 177003 (2002)
28. Y.J. Kim, J.P. Hill, H. Benthien, F.H.L. Essler, E. Jeckelmann, H. SW. Choi, T.W. Noh, N. Motoyama, K.M. Kojima, S. Uchida, D. Casa, T. Gog, Phys. Rev. Lett. **92**, 137402 (2004)
29. Y.J. Kim, J.P. Hill, F.C. Chou, D. Casa, T. Gog, C.T. Venkataraman, Phys. Rev. B **69**, 155105 (2004)
30. Y.J. Kim, J.P. Hill, S. Komiya, Y. Ando, D. Casa, T. Got, C.T. Venkataraman, Phys. Rev. B **70**, 94524 (2004)
31. Y.-J. Kim, J.P. Hill, G.D. Gu, F.C. Chou, S. Wakimoto, R.J. Birgenau, S. Komiya, Y. Ando, N. Motoyama, K.M. Kojima, S. Uchida, D. Casa, T. Gog, Phys. Rev. B **70**, 205128 (2004)
32. W.A. Harrison, *Electronic Structure and the Properties of Solids* (Dover, New York, 1989)
33. L.-C. Duda, J. Downes, C. McGuinness, T. Schmitt, A. Augustsson, K.E. Smith, G. Dhalenne, A. Revcolevschi, Phys. Rev. B **61**, 4186 (2000)
34. K. Okada, A. Kotani, Phys. Rev. B **65**, 144530 (2002)
35. Y. Harada, K. Okada, R. Eguchi, A. Kotani, H. Takagi, T. Takeuchi, S. Shin, Phys. Rev. B **66**, 165104 (2002)
36. K. Okada, A. Kotani J. Phys. Soc. Jpn. **72**, 797 (2003)
37. S.M. Butorin, J. Guo, N. Wassdahl, E.J. Nordgren, J. Electron Spectrosc. Relat. Phenom. **110-111**, 235 (2000)
38. F.M.F. de Groot, J.C. Fuggle, B.T. Thole, G.A. Sawatzky, Phys. Rev. B **41**, 928 (1990)
39. T. Idé, A. Kotani, J. Phys. Soc. Jpn. **67**, 3621 (1998)
40. S.M. Butorin, D.C. Mancini, J.-H. Guo, N. Wassdahl, J. Nordgren, M. Nakazawa, S. Tanaka, T. Uozumi, A. Kotani, Y. Ma, K.E. Myano, B.A. Karlin, D.K. Shuh, Phys. Rev. Lett. **77**, 574 (1996)
41. J. Jiménez-Mier, J. van Ek, D.L. Ederer, T.A. Callcott, J. Jia, J. Carlisle, L. Terminello, A. Asfaw, R.C. Perera, Phys. Rev. B **59**, 2649 (1999)
42. M. Matsubara, T. Uozumi, A. Kotani, Y. Harada, S. Shin, J. Phys. Soc. Jpn. **69**, 1558 (2000)
43. Y. Harada, T. Kinugasa, R. Eguchi, M. Matsubara, A. Kotani, W. Watanabe, A. Yagishita, S. Shin, Phys. Rev. **61**, 12854 (2000)
44. K. Okada, A. Kotani, J. Electron Spectrosc. Relat. Phenom. **62**, 131 (1993)
45. T. Idé, A. Kotani, J. Phys. Soc. Jpn. **67**, 3621 (1998)
46. T. Idé, A. Kotani, J. Phys. Soc. Jpn. **69**, 1895 (2000)
47. M. Matsubara, Y. Harada, S. Shin, T. Uozumi, A. Kotani, J. Phys. Soc. Jpn. **73**, 711 (2004)
48. M. Nakazawa, H. Ogasawara, A. Kotani, J. Phys. Soc. Jpn. **69**, 4071 (2000)
49. M. Watanabe, Y. Harada, M. Nakazawa, Y. Ishiwata, R. Eguchi, T. Takeuchi, A. Kotani, S. Shin, Surf. Rev. Lett. **9**, 983 (2002)
50. A. Kotani, T. Jo, J.C. Parlebas, Adv. Phys. **37**, 37 (1988)
51. M. Nakazawa, A. Kotani, J. Phys. Soc. Jpn. **71**, 2804 (2002)
52. C. Dallera, M. Marcon, G. Ghiringhelli, A. Tagliaferri, N.B. Brooks, G. Olcese, A. Palenzona, L. Braicovich, Solid State Commun. **121**, 635 (2002)
53. C. Dallera, M. Grioni, A. Palenzona, M. Taguchi, E. Annesse, G. Ghiringhelli, A. Tagliaferri, N.B. Brookes, Th. Neisius, L. Braicovich, Phys. Rev. B **70**, 85112 (2004)

54. M. Magnuson, S.M. Butorin, J.-H. Guo, A. Agui, J. Nordgren, H. Ogasawara, A. Kotani, T. Takahashi, S. Kunii, Phys. Rev. B **63**, 75101 (2001)
55. M. Matsubara, T. Uozumi, A. Kotani, Y. Harada, S. Shin, J. Phys. Soc. Jpn. **71**, 347 (2002)
56. T. Schmitt, L.-C. Duda, A. Augustsson, J.-H. Guo, J. Nordgren, J.E. Downes, C. McGuinness, K.E. Smith, G. Dhalenne, A. Revcolevschi, M. Klemm, S. Horn, Surf. Rev. Lett. **9**, 1369 (2002)
57. T. Schmitt, L.-C. Duda, M. Matsubara, A. Augustsson, F. Trif, J.-H. Guo, L. Gridneva, T. Uozumi, A. Kotani, J. Nordgren, J. Alloys Comp. **362**, 143 (2004)
58. T. Schmitt, L.-C. Duda, M. Matsubara, M. Mattesini, M. Klemm, A. Augustsson, J.-H. Guo, T. Uozumi, S. Horn, R. Ahuja, A. Kotani, J. Nordgren, Phys. Rev. B **69**, 125103 (2004)
59. G.P. Zhang, T.A. Callcott, G.T. Woods, L. Lin, B. Sale, D. Mandrus, J. He, Phys. Rev. Lett. **88**, 77401 (2002)
60. L.-C. Duda, T. Schmitt, J. Nordgren, P. Kuiper, G. Dhalenne, A. Revcolevschi, Phys. Rev. Lett. **93**, 169701 (2004)
61. M. van Veenendaal, A.J. Fedro, Phys. Rev. Lett. **92**, 219701 (2004)
62. G.P. Zhang, T.A. Callcott, G.T. Woods, L. Lin, B. Sales, D. Mandrus, J. He, Phys. Rev. Lett. **93**, 169702 (2004)
63. T. Inami, T. Fukuda, J. Mizuki, S. Ishihara, H. Kondo, H. Nakao, T. Matsumura, K. Hirota, Y. Murakami, S. Maekawa, Y. Endoh, Phys. Rev. B **67**, 45108 (2003)
64. M. Magnuson, S.M. Butorin, J.-H. Guo, J. Nordgren, Phys. Rev. B **65**, 205106 (2002)
65. M. Magnuson, S.M. Butorin, C. Såthe, J. Nordgren, P. Ravindran, Europhys. Lett. **68**, 289 (2004)
66. L. Braicovich, M. Taguchi, F. Borgatti, G. Ghiringhelli, A. Tagliaferri, N. B. Brookes, T. Uozumi, A. Kotani, Phys. Rev. B **63**, 245115 (2001)
67. M. Taguchi, L. Braicovich, F. Borgatti, G. Ghiringhelli, A. Tagliaferri, N.B. Brookes, T. Uozumi, A. Kotani, Phys. Rev. B **63**, 245114 (2001)
68. M. Taguchi, L. Braicovich, E. Annese, C. Dallera, G. Ghiringhelli, A. Tagliaferri, N.B. Brookes, Phys. Rev. B **69**, 212414 (2004)
69. H. Ishii, Y. Ishiwata, R. Eguchi, Y. Harada, M. Watanabe, A. Chainani, S. Shin, J. Phys. Soc. Jpn. **70**, 1813 (2001)
70. M. Magnuson, S.M. Butorin, A. Agui, J. Nordgren, J. Phys.: Condens. Matter **14**, 3669 (2002)
71. S. Butorin, J. Electron Spectrosc. Relat. Phenom. **110-111**, 213 (2000)
72. S. Tanaka, Y. Kayanuma, A. Kotani, J. Phys. Soc. Jpn. **59**, 1488 (1990)
73. M. Matsubara, T. Uozumi, A. Kotani, J.C. Parlebas, J. Phys. Soc. Jpn. **74**, 2052 (2005)
74. G. Ghiringhelli, presented in the *5th International Conference on Inelastic X-Ray Scattering*, Argonne (2004)
75. C.-C. Kao, W.A.L. Caliebe, J.B. Hastings, J.-M. Gille, Phys. Rev. B **54**, 16361 (1996)
76. A. Shukla, J.-P. Rueff, J. Badro, G. Vanko, A. Mattila, F.M.F. de Groot, F. Sette, Phys. Rev. B **67**, 81101(R) (2003)
77. H.-K. Mao, C.C. Kao, R.J. Hemley, J. Phys.: Condens. Matter **13**, 7847 (2001)
78. J.P. Rueff, C.-C. Kao, V.V. Struzhkin, J. Badro, J. Shu, R.J. Hemley, H.K. Mao, Phys. Rev. Lett. **82**, 3284 (1999)
79. J. Badro, V.V. Struzhkin, J. Shu, R.J. Hemley, H.K. Mao, C.-C. Kao, J.P. Rueff, Phys. Rev. Lett. **83**, 4101 (1999)
80. J. Badro, G. Fiquet, V.V. Struzhkin, M. Somayakulu, H.K. Mao, G. Shen, T. Le Bihan, Phys. Rev. Lett. **89**, 205504 (2002)
81. J. Badro, G. Fiquet, F. Guyot, J.-P. Rueff, V.V. Struzhkin, G. Vankó, G. Monaco, Science **300**, 789 (2003)
82. K. Hämäläinen, D.P. Siddons, J.B. Hastings, L.E. Berman, Phys. Rev. Lett. **67**, 2850 (1991)
83. S. Tanaka, K. Okada, A. Kotani, J. Phys. Soc. Jpn. **63**, 2780 (1994)
84. P. Carra, M. Fabrizio, B.T. Thole, Phys. Rev. Lett. **74**, 3700 (1995)
85. F. Bartolomé, J.M. Tonnerre, L. Sève, D. Raoux, J. Chaboy, L.M. García, M. Krisch, C.C. Kao, Phys. Rev. Lett. **79**, 3775 (1997)
86. F. Bartolomé, M. Krisch, D. Raoux, J.M. Tonnerre, Phys. Rev. B **60**, 13497 (1999)
87. L. Journel, J.-M. Mariot, J.-P. Rueff, C.F. Hague, G. Krill, M. Nakazawa, A. Kotani, A. Rogalev, F. Wilhelm, J.-P. Kappler, G. Schmerber, Phys. Rev. B **66**, 45106 (2002)
88. M. Nakazawa, K. Fukui, H. Ogasawara, A. Kotani, C.F. Hague, Phys. Rev. B **66**, 113104 (2002)
89. J.-P Rueff, L. Journel, P.-E. Petit, F. Farges, Phys. Rev. B **69**, 235107 (2004)
90. H. Hayashi, Y. Udagawa, W.A. Caliebe, C.-C. Kao, Phys. Rev. B **66**, 33105 (2002)
91. H. Hayashi, R. Takeda, Y. Udagawa, T. Nakamura, H. Miyagawa, H. Shoji, S. Nanao, N. Kawamura, Phys. Rev. B **68**, 45122 (2003)
92. H. Hayashi, R. Takeda, M. Kawata, Y. Udagawa, Y. Watanabe, T. Takano, S. Nanao, N. Kawamura, T. Uefuji, K. Yamada, J. Electron Spectrosc. Relat. Phenon. **136**, 199 (2004)
93. J. Tulkki, T. Åberg, J. Phys. B **15**, L433 (1982)
94. H. Hayashi, M. Kawata, R. Takeda, Y. Udagawa, Y. Watanabe, T. Takano, S. Nanao, N. Kawamura, J. Electron Spectrosc. Relat. Phenon. **136**, 191 (2004)
95. H. Hayashi, M. Kawata, Y. Udagawa, N. Kawamura, S. Nanao, Phys. Rev. B **70**, 134427 (2004)
96. M. Taguchi, J.C. Parlebas, T. Uozumi, A. Kotani, C.-C. Kao, Phys. Rev. B **61**, 2553 (2000)
97. H. Shoji, M. Taguchi, E. Hirai, T. Iwazumi, A. Kotani, S. Nanao, Y. Isozumi, J. Phys. Soc. Jpn. **72**, 1560 (2003)
98. H. Hayashi, R. Takeda, M. Kawata, Y. Udagawa, N. Kawamura, Y. Watanabe, S. Nanao, Phys. Rev. B **70**, 155113 (2004)
99. J.-P. Rueff, C.F. Hague, J.-M. Mariot, L. Journel, R. Delaunay, J.-P. Kappler, G. Schmerber, A. Derory, N. Jaouen, G. Krill, Phys. Rev. Lett. **93**, 67402 (2004)
100. M.B. Zölfl, I.A. Nekrasov, Th. Pruschke, V.I. Anisimov, J. Keller, Phys. Rev. Lett. **87**, 276403 (2001)
101. K. Held, A.K. McMahan, R.T. Scalettar, Phys. Rev. Lett. **87**, 276404 (2001)
102. C. Dallera, M. Grioni, A. Shukla, G. Vankó. J.L. Sarrao, J.P. Rueff, D.L. Cox, Phys. Rev. Lett. **88**, 196403 (2002)
103. C. Dallera, E. Annese, J.-P. Rueff, A. Pelenzona, G. Vankó, L. Braicovich, A. Shukla, M. Grioni, Phys. Rev. B **68**, 245114 (2003)

104. L.-C. Duda, J. Electron Spectrosc. Relat. Phenom. **110-111**, 287 (2000)
105. K. Fukui, H. Ogasawara, A. Kotani, T. Iwazumi, H. Shoji, T. Nakamura, J. Phys. Soc. Jpn. **70**, 1230 (2001)
106. K. Fukui, H. Ogasawara, A. Kotani, T. Iwazumi, H. Shoji, T. Nakamura, J. Phys. Soc. Jpn. **70**, 3457 (2001)
107. H. Ogasawara, K. Fukui, M. Matsubara, J. Electron Spectrosc. Relat. Phenom. **136**, 161 (2004)
108. P. Ferriani, C.M. Bertoni, G. Ferrari, Phys. Rev. B **69**, 104433 (2004)
109. K. Fukui, A. Kotani, J. Phys. Soc. Jpn. **73**, 1059 (2004)
110. K. Asakura, K. Fukui, H. Ogasawara, I. Harada, J.C. Parlebas, A. Kotani, J. Phys. Soc. Jpn. **73**, 2008 (2004)
111. K. Asakura, A. Kotani, I. Harada, J. Phys. Soc. Jpn. **74**, 1328 (2005)
112. C. Giorgetti, S. Pizzini, E. Dartyge, A. Fontaine, F. Baudelet, C. Brouder, Ph. Bauer, G. Krill, S. Miraglia, D. Fruchart, J.P. Kappler, Phys. Rev. B **48**, 12732 (1993)
113. L. Braicovich, G. van der Laan, G. Ghiringhelli, A. Tagliaferri, M.A. van Veenendaal, N.B. Brookes, M.M. Chervinskii, C. Dallera, B. De Michelis, H.A. Dürr, Phys. Rev. Lett. **82**, 1566 (1999)
114. B.T. Thole, H.A. Dürr, G. van der Laan, Phys. Rev. Lett. **74**, 2371 (1995)
115. T. Nakamura, H. Shoji, E. Hirai, S. Nanao, K. Fukui, H. Ogasawara, A. Kotani, T. Iwazumi, I. Harada, R. Katano, Y. Isozumi, Phys. Rev. B **67**, 94439 (2003)
116. J.J. Sakurai, *Advanced Quantum Mechanics* (Addison-Wesley, Reading, MA, 1967), Chap. 2
117. L. Braicovich, A. Tagliaferri, G. van der Laan, G. Ghiringhelli, N.B. Brookes, Phys. Rev. Lett. **90**, 117401 (2003)
118. G. van der Laan, B.T. Thole, J. Phys.: Condens. Matter **7**, 9947 (1995)
119. G. van der Laan, G. Ghiringhelli, A. Tagliaferri, N.B. Brookes, L. Braicovich, Phys. Rev. B **69**, 104427 (2004)